UNIVERSITÀ DEGLI STUDI DI CATANIA
Facoltà di Scienze Matematiche, Fisiche e Naturali
DOTTORATO DI RICERCA IN INFORMATICA

PROBABILISTIC MODELLING OF LAVA FLOW HAZARD AT MOUNT ETNA

ANNALISA CAPPELLO

A dissertation submitted in partial fulfillment of the requirements for the degree of "Research Doctorate in Computer Science"

COORDINATOR
Prof. Domenico Cantone

ADVISORS
Prof. Giovanni Gallo
Dr. Ciro Del Negro

XXV cycle

Acknowledgments

During my Ph.D. studies I have been accompanied and supported by many people who gave me helpful advice and practical assistance. I want to thank all of them, including those not mentioned here by name.

First of all, I would like to express my deepest gratitude to my advisors: Dr. Ciro Del Negro for introducing me to the interesting field of volcanic hazard assessment, for his valuable guidance and constant encouragement; Prof. Giovanni Gallo for the interest he has shown in my research, for his blind trust and endless support.

I am indebted to Istituto Nazionale di Geofisica e Vulcanologia for providing generous financial support throughout the Ph.D.

Acknowledgments

I am grateful to the members of the "Unità Funzionale Gravimetria e Magnetismo" for giving me generous advice and a real opportunity to learn from their experience. In particular, I wish to thank Anna for her intellectual input to my research, and Tania for her notable qualities both in scientific and personal terms.

A sincere thank goes to my flatmates – Elisa, Simona, Chiara and Annalisa – for helping me to get through the difficult times and for all emotional support, fellowship, entertainment and care provided during these three years.

I deeply thank my family and Michele, to whom I dedicate this work. Without their support, everything would have been impossible.

Finally, I can never thank Prof. Anile enough for continuing to keep a close watch over me.

Index

Introduction

Our understanding of the physical processes and parameters involved in evolution of volcanic flows is now advanced, and sophisticated process-oriented numerical models exist that describe eruptive processes well. There are a number of eruptions each year on Earth and many volcanoes are continuously monitored by dedicated observatories. Thus, volcanology is rich in statistical data and statistical modelling is an emergent and rapidly-growing area of interest.

This thesis aims at presenting a groundbreaking methodology for lava flow hazard assessment that represents a challenging topic in modern volcanology. Our purpose is to give a proper statistical treatment of volcanological data to allow key at-risk areas to be rapidly and appropriately identified.

Introduction

Assessment and management of volcanic hazards are important scientific, economic, and political issues, especially in densely populated areas threatened by volcanoes. Predicting the potentially affected areas of high-risk volcanic phenomena such as lava flows, debris flows or ash dispersion, is essential to support risk mitigation and land planning, in combination with laboratory and field observations.

Mt. Etna, in Sicily (Italy), is one of the most active volcanoes in the world, and during the past 400 years it erupted over sixty times from vents on its flanks, while eruptive activity at its summit has been nearly continuous. Its eruptions are often characterized by lava flows that spread along its flanks. Such eruptions can potentially reach the villages located at medium-low elevations. Even the area where the city of Catania is located was reached in the past by the flows that outpoured from eruptive fractures that opened at lower elevations. In the last century, the village of Mascali was destroyed by lava flows in 1928, while the villages of Fornazzo in 1979 and Randazzo in 1981 were threatened by lava flows. More recently, several tourist facilities have been repeatedly destroyed, with serious damage to the local economy specifically in the 2001 and 2002-2003 eruptions. For these reasons, knowing the probability of a particular site being overrun by a lava flow can be useful to assist emergency managers

during an eruption, to plan crisis response activities and to recognize communities and infrastructure at risk.

A powerful instrument to recognize the probability that a particular area could be affected by a lava flow over a specific time period is represented by the lava flow invasion hazard map.

Several hazard maps have already been proposed for Etna volcano. Some of them are based on a qualitative analysis of historical eruptions [e.g., *Andronico and Lodato*, 2005; *Behncke et al.*, 2005]; other maps estimate the lava flow invasion hazard by combining the probability of an eruption occurring anywhere on the volcano with the results of lava flow simulations. *Wadge et al.* [1994] used this approach for Mount Etna, where 380 lava flows were simulated by using both a stochastically chosen vent site and a set of parameters extracted from a library of lava flows erupted between 1763 and 1989. *Favalli et al.* [2009a; 2011] applied the same approach and obtained hazard maps by simulating the inundation areas for a large number of possible future eruptions using an empirical relationship for the maximum length of lava flows and a topography-based simulation probabilistic code. *Crisci et al.* [2010] elaborated a lava invasion susceptibility map based on the results of numerical simulations of flows erupted from a grid of 393 hypothetical vents located in the eastern sector of Etna. This grid was successively

extended by *Rongo et al.* [2011] obtaining a total number of 4290 source locations on the volcanic area.

The aim of my thesis is the development of a new methodology for assessing the lava flow invasion hazard in areas threatened by volcanoes, based on the application of a physics-based model for simulating the lava flow paths.

Recently, at the "Istituto Nazionale di Geofisica e Vulcanologia" (INGV), Section of Catania, significant progress have been made in the hazard assessment through the development of accurate and robust physical-mathematical models able to forecast the spatial and temporal evolution of lava flows. With such simulations, a large number of eruptive scenarios can be explored and used to estimate the extent of the inundation area.

In particular, the methodology for the hazard assessment is based on three main steps: (i) the construction of a spatiotemporal probability map for the future opening of new eruptive vents; (ii) the estimation of the occurrence probabilities associated to classes of expected eruptions; and (iii) the overlapping of a large number of lava flows simulated using the MAGFLOW model. The results from these steps are processed in order to obtain a hazard map showing, for a given area, the probability of being affected by at least one lava flow inundation during the time interval considered.

The preferred scenario for this study is Mt Etna being one of the most intensively monitored volcanoes in the world, thereby offering a lot of input data for the application of the proposed methodology.

Chapter 1 describes the first and maybe the most important step in forecasting lava flow hazards that is the identification of such areas most susceptible to the spatial opening of new eruptive vents at Etna, named susceptibility map. The quantitative evaluation of the probable location of future eruptions is obtained analyzing the past geological and volcanological history of Etna, introducing a recurrence rate, which defines a possible spatial vent density. However, in order to accurately assess the distribution of future vent locations, the location of past eruptive events, as well as the possible spatial shift in effusive activity, should be considered.

Chapter 2 presents a stochastic model of eruptions that combines the temporal and spatial analysis to evaluate the spatiotemporal probability of future vent opening on the flanks of Mt. Etna. The basic assumption is that the temporal patterns extracted from the records of past eruptions are useful to predict the future behaviour of a volcano, as well as the regions at high density of volcanic structures are the most probable emission zones of future lava flows. Finally, the results of the analysis of the persistent summit activity during the

last 110 years indicate that the hazard rate for eruptive events is not constant with time, differs for each summit crater of Mt Etna, highlighting a general increase in the eruptive frequency starting from the middle of last century and particularly from 1971, when the South East Crater was born.

In *Chapter 3* the approach used to characterize the expected eruption is introduced. Input data, extracted from the new geological map and from the catalogues of historical eruptions of Etna, consist of different kind of records associated to the effusive activity at Mt Etna of the past 400 years, from 1607 to 2006. In particular, information about eruption duration and the lava flow volume are used to perform a statistical analysis, from which six eruptive classes are identified. Hence an occurrence probability is estimated, which represents the probability that one of the considered classes can occur.

Chapter 4 describes the MAGFLOW simulator developed at INGV-CT. MAGFLOW is a Cellular Automata model based on physical modelling of lava flows, as its evolution function is derived from a steady-state solution of the Navier-Stokes equation for Bingham fluids, coupled with a simplified heat transfer model. On Etna, the MAGFLOW has been successfully used to reproduce lava flow paths during effusive eruptions and paroxysmal events, to consider the

impact of hypothetical protective barriers on lava flow paths and to produce the lava flow invasion hazard map at the South-East Crater. This Chapter describes the model and the results of a sensitivity analysis conducted on the physical and rheological parameters that control the evolution function of the automaton. The results confirm the overall reliability of MAGFLOW for lava flow simulations and demonstrate that, for a given composition, discharge rates strongly influence the modelled emplacement.

Chapter 5 depicts the effective construction of the hazard map, which consists in merging the spatiotemporal probability map, the event probabilities and the areas invaded by the simulated lava flows. The hazard map captures the probability of invasion of lava flows that could potentially inundate specific areas, allowing the rapid assessment of the threat posed by an eruption from a given area and thus representing a support tool for decision makers.

Finally *Chapter 6* describes a big challenge in the field of the computational assessment of volcanic risk. The hazard map by lava flow invasion constitutes the starting point for building the risk map, showing the expected value of losses due to the occurrence of an eruption in a particular area at a given time period. The construction of the risk map consists in combining the lava flow invasion hazard

map with the exposed value, which evaluates the goods on the territory that may be affected by an event. The resulting map constitutes a powerful instrument for evaluating the real cost of living in areas near Etna volcano and for overseeing long-term land use and territorial planning.

Chapter 1

Spatial vent opening probability map

Volcanoes usually erupt from the summit area, fed by the central conduit. However, many eruptions occur from vents along the volcano flanks. In some active volcanoes with open central conduit, including Kilauea, Stromboli, Vesuvio (between 1631 and 1944), and Etna, the occurrence of flank eruptions is similar or even more frequent than that of summit eruptions [*Holcomb*, 1987; *Neri and Acocella*, 2006; *Acocella et al.,* 2006, 2009; *Neri et al.,* 2011a]. These flank eruptions are usually responsible for effusive activity, which may feed lava flows capable of flowing for long distances over the volcano's slopes and invading vulnerable areas.

Forecasting the possible location of flank eruptions, in addition to any summit activity, is an important challenge to improve our understanding of volcanic processes so as to achieve successful assessments of lava flow hazards [*Newhall*, 2000; *Sparks*, 2003; *Behncke et al.,* 2005; *Crisci et al.,* 2010; *Cappello et al.,* 2011a; *Bonaccorso et al.,* 2011; *Ganci et al.,* 2012b].

Various approaches, based on statistical or probabilistic analysis of the geology and structure of a volcano and the processes driving magma transfer, were proposed to forecast the location of future eruptive vents. *Wadge et al.* [1994] evaluated a probability surface of future vent locations on Etna, starting from a classification of its flank eruptions from 1763 to 1989, and applying a non-homogeneous Poisson process. *Connor and Hill* [1995] proposed three nonhomogeneous Poisson processes to estimate the recurrence rates and the associated probability of volcanic eruption in the Yucca Mountain (Nevada). These models were extended by *Martin et al.* [2004] in a Bayesian framework applied to the Tohoku volcanic arc (Japan) to combine different geological and geophysical information assuming that new volcanoes will not form far from existing ones. Recently, *Marti and Felpeto* [2010] proposed a numerical multicriteria evaluation of the spatial probability of hosting a new crater in Tenerife (Canary Island) assigning weights (chosen through

the expert judgment elicitation) to different layers of information obtained with structural criteria (for long-term analysis) and monitoring data (for short-term analysis).

Some of these studies have a common limitation due to the not well-detailed knowledge of the volcano structure, as well as its mechanisms of shallow magma transfer, preventing the formulation of a solid theoretical base for the statistical analysis.

Recently, *Neri et al.* [2011b] completed a study on the modalities of flank eruptions at Etna of the last $\sim$2 ky, for which a detailed structural database was collected. These geological records allowed new and broader insights into the dynamics of summit and flank eruptions, defining the main structural parameters and, possibly, the role of the magmatic intrusions in the framework of the volcano flank instability. During the last hundreds of years the central conduit of Etna is always open and active; in addition, lava flows from the summit vents are incapable of threatening the villages located at medium-low altitudes on the flanks of Etna or reaching the Ionian coast where the city of Catania is located [*Behncke et al.*, 2005]. For these reasons, only flank events were analyzed to identify areas where new eruptive vents may open at Etna.

The approach proposed is based on the possibility of accounting for the available geological and structural data, highlighting the main

pathways of magma transfer, as well as an understanding of their mechanisms to derive a susceptibility map containing spatial estimates suggesting the most likely future emission zones. The operative procedure consists in converting different structural datasets (faults, dikes, and eruptive fractures) in separate probability density functions (PDFs), giving each of them a relevance value (weight) with respect to the evaluation of susceptibility, and finally combining all the PDFs and weights in a non-homogeneous Poisson process.

1.1. Geological and structural data

Etna is a basaltic volcano located on the Ionian Coast of Sicily, Italy (Figure 1). Its activity began about 0.5 Ma, when it generated submarine eruptions inside the "Pre-Etnean Gulf"; subsequently, up to ~0.2 Ma, the activity became subaerial producing fissural volcanism, and finally building the present-day central strato-volcano [*Corsaro et al.,* 2002; *Branca et al.,* 2004]. Present activity is manifested by summit eruptions, due to the ascent of magma through the central conduit, and flank eruptions, characterized by vents radiating outward from the summit. Most of flank eruptions originate from the central conduit: here magma rises and subsequently

propagates laterally and downslope, feeding lateral fissures. Less frequently, flank eruptions, named "eccentric" or "peripheral", are triggered by intrusions directly fed by different reservoirs beneath the volcano (Figure 1b) [*Acocella and Neri* 2009; *Neri et al.,* 2011a, b]..

Etna's eastern and southern flanks are characterized by slow but continuous seaward displacement (Figure 1) [*Solaro et al.*, 2010]. Northward, the unstable area is delimited by the Pernicana fault system (PFS) [*Tibaldi and Groppelli,* 2002] and to the South-West by the Ragalna fault system (RFS) [*Neri et al.,* 2007]. Recent InSAR observations reveal differential slip along faults inside the unstable area, delimiting blocks characterized by different velocity of deformation [*Solaro et al.*, 2010]. A close relationship between flank deformation and eruptive activity at Etna is described in *Bonaccorso et al.* [2006].

Distinct eruptive cycles have been observed since 1865, with flank eruptions occurring in clusters, separated by periods of quiescence and summit activity [*Behncke and Neri*, 2003]. Flank eruptions seem to occur more frequently during accelerations of flank movements, facilitated by the opening of fractures close to the summit of the volcano and by increased activity of the main fault systems [*Neri et al.,* 2009].
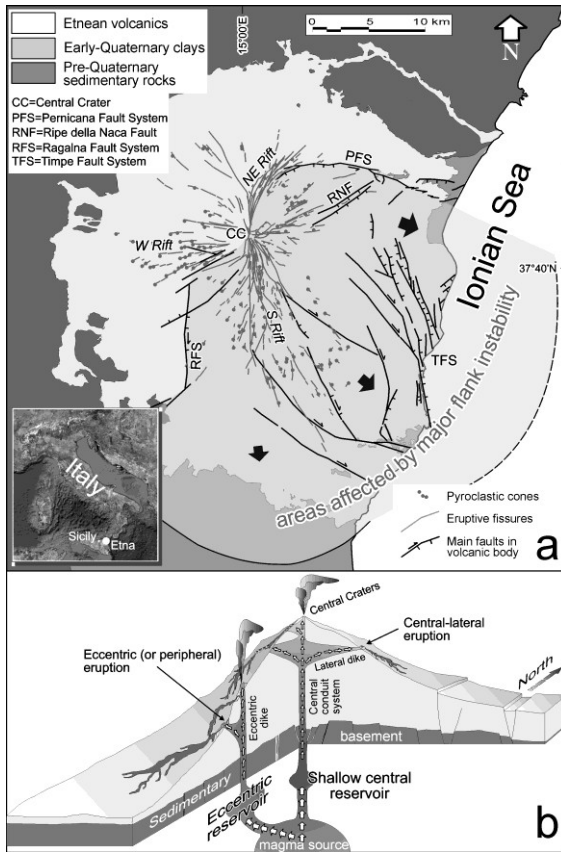
Figure 1 – Structural map of Etna: (a) distribution of eruptive fissures and pyroclastic cones produced by flank eruptions, fault systems, and the sector affected by flank instability-induced displacement (in light gray). Arrows indicate directions of movement in different portions of the mobile sector. (b) Block diagram (not to scale) illustrating the assumed geometric relationships between the two different, lateral and eccentric magma pathways established during the 2001 and 2002-03 flank eruptions.

Based on field measurements, satellite data and geophysical observations, *Neri et al.* [2011a] have completed a detailed study of the main structural features of lateral eruptions at Etna, including the frequency and strike of outcropping and buried eruptive fractures active in the past ~2 ky, of the dikes cropping out in the Valle del Bove (VdB), and of the main faults that can potentially be used as pathways for intruding magma. All these geological and structural data were used to construct a georeferenced database containing the mapping of: (1) the outcropping and buried eruptive fissures; (2) the dikes cropping out in the VdB; (3) the main faults.

Eruptive fissures

A total amount of 330 eruptive fissures, active during the last ~2 ka (Figures 2 and 3), were analyzed, Their importance lies in the fact that they are dike-fed, and dikes are the most effective means for the rise of magma in the upper crust [*Acocella and Neri*, 2009]. The way eruptive fissures propagate allowed distinguishing "central-lateral" dikes (propagating laterally from the central conduit) from "peripheral" or "eccentric" dikes, not connected to the central conduit. Since only three eccentric eruptions occurred in the last 110 years [*Behncke et al.*, 2005] and it is difficult to recognize oldest

eccentric eruptions, they have been not distinguished from the other lateral eruptions.
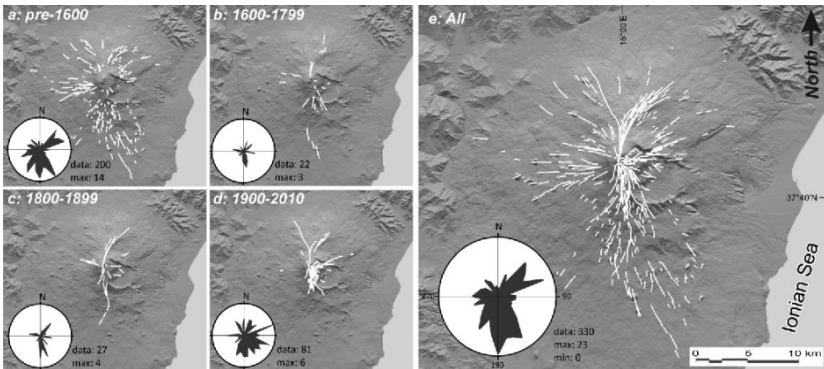
Figure 2 – Historical eruptive fissures of Etna, grouped into periods: pre-1600 (a), 17th and 18th centuries (b), 19th century (c), 1900-2010 (d), and all fissures plotted together (e). Rose diagrams report the geometric orientation of fissures for each period (redrawn from Neri et al. 2011a).

At higher altitudes (>2000 m), almost all eruptive fissures are radial with respect to the volcano summit. However, these radial fissures cluster along an overall ~N-S trend, that is perpendicular to the direction of regional extension in the area.
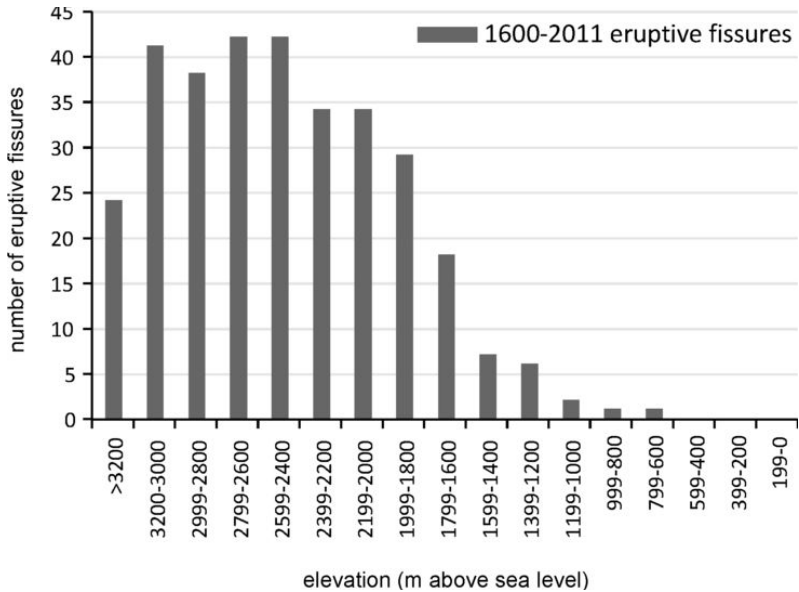
Figure 3 – Distribution of the post-1600 eruptive fissures of Etna, grouped into different altimetric intervals. About 90% of the fissures are distributed between the summit and 1800 m a.s.l., with ~60% located above 2400 m.

At lower altitudes (<2000 m) a few of the longest fissures (> 5 km) propagating downslope are rotated by 10°-40° with regard to the radial path. The vast majority (~96%) of the entire fissure population is radial, with a negligible population (~4%) slightly deviating from

the radial path. These latter fissures, located at the lower extremities of the North-East and South Rifts, mainly show NE and SE directions, respectively (Figure 2). These directions are consistent with those of the nearby structures controlling the slip of the unstable eastern flank of the volcano [*Solaro et al.*, 2010], so that a relation between eruptive activity and flank instability may be expected at these lower altitudes.

Fissures older than 1600 are uncertain in age and were inserted into the same georeferenced layer (Figure 2a). This group includes 200 fissures, largely with a S-ward (43% of the cases), NE-ward (23%) and W-ward (20.5%) direction.

Sixty-six flank eruptions and 130 fissure systems were identified between 1600 and 2011. Nineteen of these eruptions occurred during the 17th and 18th centuries, generating 22 fissures (Figure 2b; in some cases, the same eruption produced multiple eruptive systems with different orientations). Thirteen flank eruptions formed 27 fissures during the 19th century (Figure 2c). Twenty-seven and six events in the 20th and 21st centuries, respectively, generated 81 fissures (Figure 2d). The total of fissures is oriented with a S-ward (39% of the cases), NE-ward (22%) E-ward (18%), and W-ward (11%) direction, and a minor percentage with a N-S orientation (8%). The frequency distribution of the post-1600 eruptive systems shows

that ~60% are located above 2400 m, 30% crops out in between 1800 m and 2400 m, and the remnant 10% are below 1800 m a.s.l.

Dikes

Dikes outcropping in VdB, consisting of radial, tangential and oblique systems, were analyzed and integrated in a georeferenced map (Figure 4).

Radial dikes predominate, confirming what has been observed from radial fissures mapped at the surface. However, while at the surface dikes show a systematic radial configuration, at depths of several hundreds of meters, in areas exposed by erosion in VdB, tangential and oblique dikes are also present.

Analogue models show how dikes approaching the flanks of cones [*Neri et al.,* 2008; *Acocella et al.,* 2009], regardless of their initial orientation, reorient to become radial (parallel to the maximum gravitational stress; Figure 4b). This reorientation is a significant process in shallow magma migration and is expected to control also the emplacement of the dike-fed fissures reaching the lower slopes of the volcano.
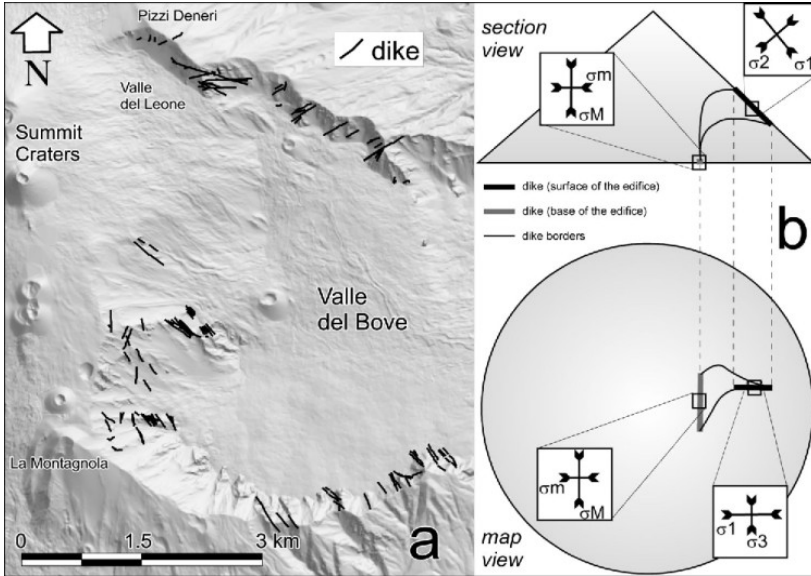
Figure 4 – Dikes cropping out in VdB following the present-day structural trends (a). Schematic representation of possible dike reorientation upon approaching the surface of a cone, in map and section views (b). At the base of the cone, the attitude of the dike depends upon the regional stress field, characterized by a maximum (σM) and minimum (σm) principal stress, as shown by the insets. At the topographic surface, the load of the cone re-orients the dike, in accordance with the three principal gravitational stresses (local σ1, σ2 and σ3), as shown in the insets (after *Acocella et al.,* 2009).

Irrespective of their initial attitude, radial dikes (clustering along a regional ~N-S trend) are expected to feed most of the eruptive activity along the slopes of a composite volcano as Etna. Since only a negligible portion (4%) of the eruptive fissures is not radial, only the dikes with a radial pattern were considered as those capable of transferring magma to the surface, and thus to feed flank eruptions.

Faults related to eruptive fissures

Georeferenced mapping of Etna faults has been carried out, merging field, seismic and magnetotelluric data [*Cardaci et al.,* 1993; *Monaco et al.*, 2008; *Bonforte et al.* 2009; *Falsaperla et al.,* 2010; *Siniscalchi et al.,* 2012] with structural data acquired through satellites [*Solaro et al.,* 2010] and geochemical mapping [*Siniscalchi et al.,* 2010; *Neri et al.,* 2011b].

The faults considered were those possibly involved in the eruptive processes, both actively (when they promote upraise and propagation of dikes) and passively (when they are intersected by shallow sub-horizontal or slightly inclined dikes, allowing the magma to rise along their dislocation planes). These faults were highlighted by seismic, tomography, geodetic, and magnetotelluric studies [*Cardaci et al.,* 1993; *Solaro et al.,* 2010; *Siniscalchi et al.,* 2012].

In particular, two types of faults (yellow lines in Figure 5) were identified: (i) faults departing from the summit area, and frequently serving as pathways for dikes that propagate from the central conduit toward the volcano periphery; they are largely radial and crop out in few cases because of they are often buried by recent eruptive products; (ii) faults that, due to their position, can be intersected by the sub-horizontal propagation of shallow radial dikes and host the passive emplacement of magma (i.e., during the 1928 eruption the lower vents opened at the point where the shallow dike propagating downslope from the central conduit in NE direction intercepted the Ripe della Naca fault plane; Figure 1); because of their distal location and general lack of a radial attitude, these faults are not expected to significantly control the location of eruptive vents. This group also includes faults that, being part of the network of structures characterizing the flank instability, might facilitate upraise and eruption of magma ("passive eruptions", i.e. not determined simply by magmatic overpressure but mainly by external factors).

For instance, the purely effusive 2004-2005 eruption was triggered by the intersection of the fracture system bordering the sector of the volcano affected by flank instability, with the Southeast Crater plumbing system, leading to the draining of magma [*Neri and Acocella*, 2006]; the event demonstrates that lateral spreading of

Etna's eastern flank can trigger geodynamically-controlled eruptions [*Burton et al.*, 2005, *Neri and Acocella*, 2006].

Figure 5 shows that, except for the Timpe Fault System (to the east) and a few minor faults on the W flank, most of the active faults are located along the peripheral continuation of the North-East and South Rifts. Also, almost all the tectonic deformation at the end of the focused North-East Rift seems related to the activity of one main single fault (the Piano Provenzana fault, Figure 5, becoming to the east the Pernicana Fault) [*Ruch et al.,* 2010]; conversely, at the end of the wider S Rift, the deformation is partitioned among different fault systems. Therefore, a correlation appears between the end and width of a Rift and its continuation as a broader or narrower zone of deformation.

Moreover, there is a strong link of these faults at the termination of a rift with the instability of the W and S flanks [*Bonforte et al.*, 2011]. In some cases, there is evidence that fissure eruptions in the summit area become major faults, characterizing the activity of the Etna unstable flank, on the lower slopes (i.e. the NW-SE 1989 fissure system, which connects the summit region of the volcano with the tectonic structures of the lower SE flank) [*Falsaperla et al.,* 2010].
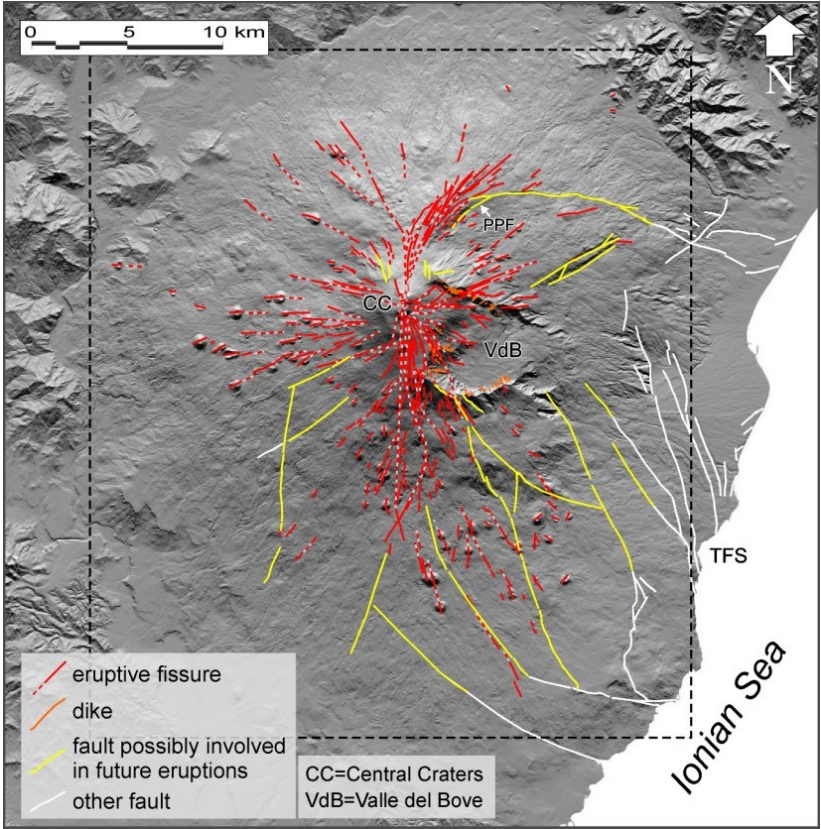
Figure 5 – Main faults and structures of Etna. Dashed red lines indicate dry (or poorly active) segments of the eruptive fracture systems. Black box indicates the area of ~36×32.5 km containing the 500 m grid spacing of potential vents. TFS = Timpe Fault System; PPF = Piano Provenzana fault.

The more focused deformation controlling flank instability on the N boundary (PFS) matches with the narrower North-East Rift and contrasts the more diffused deformation of the unstable flank to the south, matching with the wider South Rift.

All these features suggest a link between the location and activity of the North-East and South Rifts and the instability of the E and S flanks of the volcano. It is expected that, on the upper slope, gravity and magma emplacement play a common role, feeding each other and justifying the preferred magmatic activity along the North-East and South Rifts.

1.2. The probabilistic model

The qualitative analysis of the structural features of Etna eruptions provides the theoretical background to explain and motivate the prediction of the future vent opening by any probabilistic model:

a) most of the new fissures are expected to be radial and focus above 1600 m;

b) control of the regional tectonics suggests that numerous fissures (~36%) are expected to have an overall ~N-S trend, therefore to develop along the South Rift;

c) a link between flank instability and the occurrence of fissure eruptions along the North-East and South Rifts is expected as result of the gravitational instability of the E and S flanks.

Moreover, some reasonable assumptions can be made about the contribution of each structural dataset to construct the susceptibility map. In principle, the most importance is given to recent (post-1600) eruptive fractures, considering them as the current, main expression of the volcano structure related to the eruptions. The contribution of the other datasets is considered less important (pre-1600 eruptive fractures), or considerably less important (faults and dikes), because of their "passive" role in the intrusion processes (faults) and their age (dikes).

To translate these qualitative assumptions into a mathematical language, the spatial distribution of past volcanic structures, such as faults, dikes, and eruptive fractures divided by age, were initially converted into separate PDFs. Successively, through a back analysis, each PDF is assigned a weight, measuring the importance and quality of data. Finally, the PDFs and their relative weights are combined via a weighted summation and modeled in a non-homogeneous Poisson process to obtain the susceptibility map.

Probability estimations based on kernel technique

The structural georeferenced database of Etna includes four datasets: eruptive fissures of the past ~2 ky (separated per age into two datasets, pre-1600 and post-1600 fissures), dikes cropping out in the VdB, and main tectonic structures that can potentially be used as pathways for intruding magma and/or influence the superficial stress field of the volcano, namely faults.

A 500-m spaced grid of potential vents $v_i(x,y)$ was defined over an area of 36×32.5 km (Figure 5), and, after proving the divergence of the spatial distribution from randomness for all four datasets with the R-score [*Clark and Evans*, 1954], a probability of activation (p_a) was assigned to each potential vent $v_i(x,y)$ through a non-homogeneous Poisson process:

$$p_a(v_i) = 1 - e^{-\Lambda(x,y)\Delta x\Delta y} \tag{1}$$

where $\Delta x\Delta y$ is the dimension of the grid cell (0.25 km^2), and $\Lambda(x,y)$ is the total expected recurrence rate per unit area, calculated by summing the products of the local intensity function λ_{xy} for the *s*-th dataset and its relative weight *w(s)*.

$$\Lambda(x, y) = \sum_{s=1}^{S}\left(\lambda_{xy}(s) * w(s)\right) \tag{2}$$

The local intensity function λ_{xy} was computed using a kernel function, which is presently the most feasible tool for probabilistic modelling of the long-term future patterns of volcanic events. A kernel function is a PDF centered at each data sample location while exerting an influence in the surrounding region [*Diggle*, 1985]. It is employed to calculate the probability surface from the location of past, discrete events, in function of distance to nearest-neighbors and a smoothing factor.

Different kernels can be used to describe the spatial density, such as the Cauchy kernel [*Martin et al.,* 2004], the Epanechnikov kernel [*Lutz and Gutmann,* 1995], the Gaussian kernel [*Connor and Hill,* 1995], and an elliptical kernel [*Kiyosugi et al.,* 2010]. To assess the spatial probability of future events at Etna, a Gaussian kernel was employed since this model responds well to clustering phenomena commonly observed in volcanic distributions [*Weller et al.*, 2006]. The formula of the Gaussian kernel is given by:

$$\lambda_{xy} = \sum_{j=1}^{N} e^{-\frac{d_j^2}{2h^2}} \tag{3}$$

where N is the number of structures, h is the smoothing factor, and d_j represents the minimum distance among those calculated between the potential vent $v_i(x,y)$ and each segment constituting the j-th volcanic structure.

The kernel λ_{xy} is then normalized so that its integral across the whole area is unity.

Choice of the smoothing parameter

The smoothing parameter h strongly influences the result of the kernel function, controlling how λ_{xy} varies with distance from existing volcanic structures. If h is small, the estimated probabilities are high in proximity to existing structures, but low away from the structure. Conversely, a large value of h yields a more uniform estimate of probability distribution across the region. In a volcanic context, the choice of h depends on several factors, including the volcanic field size and degree of clustering.

To select the smoothing parameter, the explicit version of the Least Squares Cross-Validation (LSCV) was used, which is based on minimizing the integrated square error between the true and an estimated distribution [*Worton*, 1995]:

$$LSCV(h) = \frac{1}{\pi h^2 N} + \frac{1}{4\pi h^2 N^2} \sum_{i=1}^{N} \sum_{j=1}^{N} \left(e^{-\frac{d_{ij}^2}{4h^2}} - 4e^{-\frac{d_{ij}^2}{2h^2}} \right) \qquad (4)$$

being N the number of structures and d_{ij} the "minimax distance", that is the minimum value of the maximum distances between each end point of the i-th structure and all the end points of the j-th volcanic structure.

Varying the value of h in Equation 4, it was found that the smoothing factors minimizing the LSCV(h) score for each dataset are: 1050 m for dikes, 1350 m for faults, 1200 m for pre-1660 fissures, and 1000 m for post-1660 fissures. These h values were then used in Equation 3 to convert each dataset in a PDF (Figure 6).
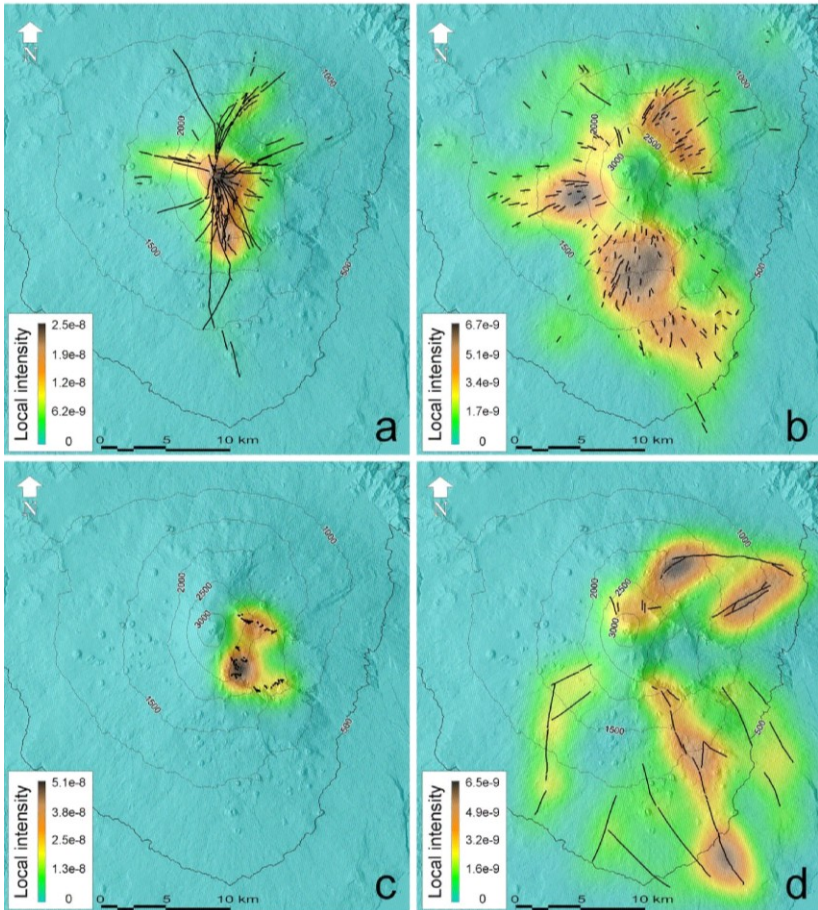
Figure 6 – PDFs for post-1600 fractures (a), pre-1600 fractures (b), dikes (c) and faults (d) calculated with a Gaussian kernel.

Back analysis for weights selection

To assign a weight to each PDF, an unbiased procedure was used for the back analysis, which generally aims to determine parameters and/or properties on the basis of a sample of known data. In terms of volcanic susceptibility, it is employed to identify how historical structural data have affected the most recent eruptions.

Taking into account the age of the eruptions, all the structural data were divided in two parts, using the first one as learning set and the second one as testing set.

The year 1981 was fixed as a time barrier, since it determines two statistically meaningful sets (49 fissures for learning and 10 for testing). Moreover, starting from 1981, the volcano activity shows an increasing temporal trend [*Salvi et al.,* 2006; *Bebbington,* 2007; *Cappello et al.,* 2011b].

Volcanic structures formed before 1981 were converted in four PDFs and a weight w(s) belonging to the interval [0.05, 0.85] was assigned to each of them to obtain 969 susceptibility maps. Eruptive fissures opened after 1981 (Figure 7) were employed to find the best weights through an exhaustive research of the maximum value reached by the following performance index:

$$PI = \frac{100}{N*p_{max}} \sum_{i=1}^{N} p_i \qquad (5)$$

where p_i is the probability of the i-th testing fissure, p_{max} is the highest probability, and N is the number of testing events.
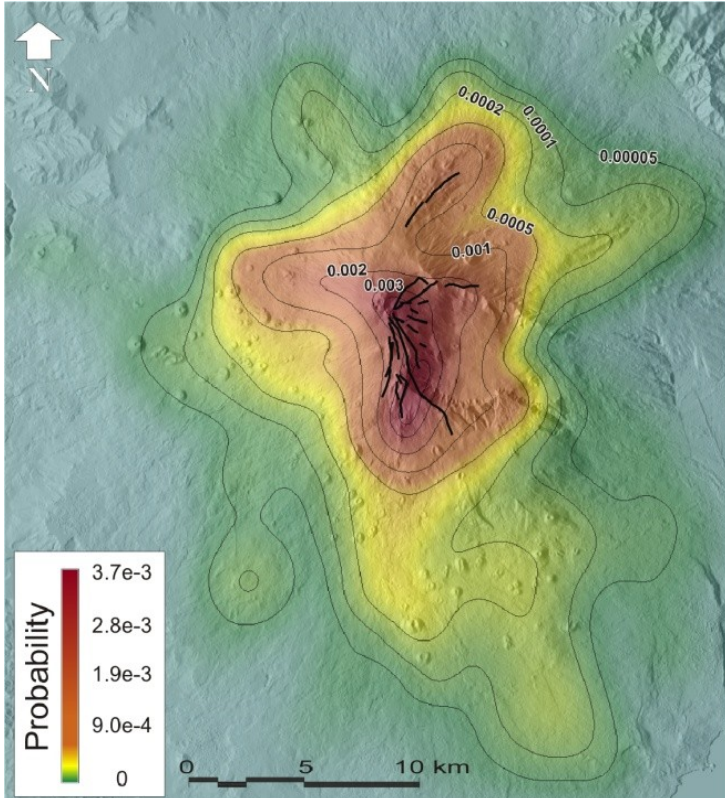

Figure 7 – Eruptive fissures (black lines) related to the ten eruptions (from 1983 to 2008-09) considered as testing dataset to estimate the weight of each PDF. Locations of fissures are superimposed on the susceptibility map evaluated with structural information until 1981.

PI is a percentage representing how the post-1981 fissures are close to the maximum probability. The highest value of PI (~77.3%) was obtained assigning 0.10 to faults, 0.15 to dikes, 0.15 to pre-1600 fissures, and 0.60 to post-1600 fissures. The weighted summation of the PDFs was then inserted into Equation 1 to obtain the quantitative evaluation of the probability of new vents opening in the Etna area.

1.3. Results

The final susceptibility map is shown in Figure 8.

The zone with the highest probability of new vents opening is centered on the summit crater area and radially around it, to ~2900 m a.s.l. These summit eruptive fractures are related to the dynamic of the central crater area, which is characterized by (i) paroxysmal episodes lasting a few hours; (ii) lava overflows of longer duration (days to months) from the summit craters; and (iii) effusive events from fractures on the external flanks of the summit cones, most of which do not propagate at lower altitudes, due to the superficial nature of the magmatic intrusions.
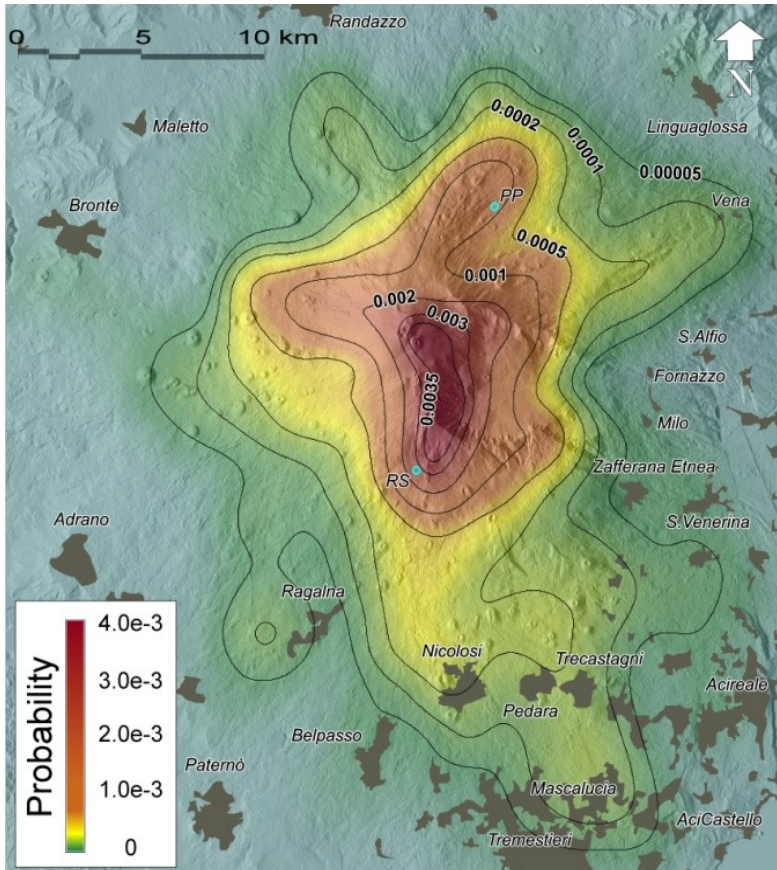
Figure 8 – Susceptibility map at Etna. The highest probability of new vent opening regards the N-S aligned area passing through the Summit Craters down to ~2000 m a.s.l. High probabilities are also evident in the NE, W and S Rifts, and the ENE flanks. RS = Rifugio Sapienza; PP = Piano Provenzana.

The distribution of the summit craters, four of them to date, seems to be controlled by two main structural trends, oriented SSW-NNE and NW-SE, respectively: NNE from the Voragine one encounters the North-East Crater (born in 1911), at the northern base of which begins the Northeast Rift, whereas going SE from the Voragine, one encounters the Southeast Crater (born in 1971), which in turn overlooks the upper portion of the South Rift zone.

The position of Bocca Nuova (born in 1968) is less clear; the volcano-tectonic structures within the Bocca Nuova, often oriented N-S and NNW-SSE, seem to point to a dynamic link to the Central Crater, the huge, single summit crater that existed during the first half of the 20th Century, and within which the Voragine and Bocca Nuova have developed.

The four summit craters have sometimes shown contemporaneous eruptive activity, but with different style and eruption rates. This implies a structural independence of the respective feeder conduits in their most superficial portion (<2-3 km from the surface). Most recently, a new pyroclastic cone has started growing on the lower east flank of the South-East Crater, reaching a height of about 150 m 25 paroxysmal episodes in 2011-2012 [*Vicari et al.,* 2011b; *Ganci et al.,* 2012a].

Below 2900 m a.s.l., Figure 8 shows a N-S zone of elevated probability of new eruptive vents opening, ~7×2.5 km wide, extending from the summit area to ~1700 m altitude on the south flank. This is the uppermost portion of the South Rift, which is the strip of terrain along the western rim of the VdB.

At lower altitudes, this rift area opens fanwise toward SSE and SE, down to rather low altitude (minimum altitude ~400 m), coinciding with the most densely populated area of the volcano.

In the SE area, several NW-SE pre-1600 fissures and NW-SE faults crop out influenced the extension of the susceptible zone at lower altitude, although the low weight assigned by the performance index elaboration.

A second area (~8×2 km wide) with a high probability of new vents forming extends from the summit toward N-NE (downward to ~1000 m a.s.l.). It includes the North-East Rift, characterized by numerous eruptive fissures and pyroclastic cones. It has been active for at least 15-20 ky; in the recent past, the eruption frequency here was lower than on the S flank). Yet this rift plays a fundamental role in the structural setting of the volcano, because it represents the NW boundary of the sliding eastern flank [*Ruch et al.*, 2010].

The North-East Rift indeed shows faults and fractures characterized by predominantly extensional kinematics, which pass into left-lateral

transtensive kinematics in its lower portion, where it is linked to the transtensive left-lateral Pernicana fault system, the northern margin of the zone affected by flank instability.

Along the complex structural North-East Rift – PFS system, which is ~3-4 km deep [*Ruch et al.*, 2010], one can imagine the ascent of dikes and magmatic fluids [*Siniscalchi et al.*, 2012], which use the tectonic discontinuities as pathways to the surface, while facilitating the movement of one block against the other due to a "lubrificating" action on the fault planes. Outcropping and buried dikes and pyroclastic cones, deformed by the tectonic activity, indeed occur along the PFS around 1450 m altitude [*Tibaldi and Groppelli*, 2002], testifying to the existence of this volcano-tectonic setting. Structurally and morphologically, the North-East Rift is linked to the North-East Crater. During the 1960s to 1980s, this crater produced vast and thick lava fields, which bury much of the North-East Rift down to ~2500 m altitude.

Yet another zone of elevated probability of new vents opening extends from the summit area toward ENE. This is the East-North-East Rift [*Ruch et al.,* 2010], whose lower portion passes into the Ripa della Naca faults (~1000 m altitude), and includes the Valle del Leone and a portion of the N wall of the VdB, as well as a number of parasitic cones. Both the eruptive fissures and dikes outcropping in

this area were conditioned, during their propagation, by the presence of the N wall of the VdB, due to their shallow paths (from a few tens to a few hundreds of meters of depth). In some cases, the intrusions halted at the base of the VdB wall (as in 1989 and 2001), whereas on other occasions the fractures cut through the wall, first changing direction and adapting the trend of the wall itself, and then resuming their original direction (toward NE and ENE), thus propagating outside the VdB (as in 1971 and 1979).

Analyzing the geometric properties and structure of the dikes outcropping in the area, an identical evolution of the past eruptive activity can be inferred. The kinematic indicators present in the magmatic intrusive bodies (that is, the form and arrangement of bubbles, flow structures, morphology of the imprint of glassy margins on the host rocks) clearly indicate a subhorizontal (0-10°) or slightly inclined (10°-30°) mode of propagation of magma within the fractures [*Acocella et al.,* 2009].

Finally, another area of elevated probability of new vents opening extends from the summit toward W and WSW, downward to ~1700-1800 m a.s.l. This is the most elevated portion of the West Rift, where flank cones reach a minimum altitude of ~1300 m and most recent eruptive manifestation dates back to 1974.

Spatial vent opening probability map

Compared to the other rift zones, some geological data (significant documented explosive activity) and instrumental evidence (seismic swarms preceding some eruptions) suggest that some West Rift eruptions might have been fed directly from a deep magma reservoir, bypassing the central conduit of the volcano.

Chapter 2

Spatiotemporal probability map of vent opening

The methodology described in Chapter 1 uses only the spatial distribution of geological and structural data to estimate the probability of future events at Mount Etna. However, in order to accurately assess the distribution of future vent locations, two aspects should be considered simultaneously: the spatial density (number of volcanic events per unit area) and recurrence rates (number of volcanic events per unit time).

In other words, the probabilistic modelling of future vent opening should consider simultaneously the spatial and temporal characteristics of volcanic activity.

Different approaches have been proposed to evaluate the probability of vent opening at Etna volcano by analyzing the distribution of spatial location of flank eruptions and their temporal frequency in a separate way.

For the spatial distribution, the density of vents has been calculated to identify areas where the highest concentration is located, which correspond to the zones known as NE, S and W Rifts, respectively [*Guest and Murray,* 1979; *Acocella and Neri,* 2003; *Salvi et al.,* 2006; *Crisci et al.,* 2010; *Rongo et al.,* 2011; *Neri et al.,* 2011a; *Cappello et al.,* 2012].

For the temporal distribution of flank eruptions, *Mulargia et al.* [1985] concluded that Etna's lateral eruptions follow a stationary Poisson process with a constant intensity. *Salvi et al.* [2006] confuted this result, proving that flank eruptions at Etna do not follow a simple Poisson distribution, but are more likely represented by a non-homogeneous Poisson process with power law intensity. Recently, *Bebbington* [2007] applied the Hidden Markov Models (HMM) to volcanic occurrences to identify the most consistent (hidden) activity state of the volcano with the observations and to forecast the next eruptions. However, the stationary distribution assumed by HMM cannot properly model the increasing trend of flank eruptions observed in the last 40 years at Etna [*Allard et al.,* 2006]. Finally, the

temporal analysis performed by *Smethurst et al.* [2009] revealed that flank eruptions follow a non-homogeneous Poisson process with a piecewise intensity increasing nearly linearly since the mid-1900s.

This Chapter describes a methodology to evaluate the spatiotemporal probability of future vent opening at Mt Etna which combines both the temporal and spatial analysis of flank eruptions. The basic assumption is that the temporal patterns extracted from the records of past eruptions are useful to predict the future behaviour of a volcano, as well as the regions at high density of volcanic structures are the most probable emission zones of future lava flows.

2.1 Etna volcanic eruptions: types, frequencies and structural features

Periodic flank eruptions in the last four centuries

Before the beginning of the 17th century, the catalogue of Etna flank eruptions is fragmentary and incomplete, but since 1610 an almost complete account of eruptions is available, which has been summarized by *Sartorius von Waltershausen* [1880], *Imbo* [1928, 1965] and more recently by *Wadge* [1977].

The eruptive behavior of Etna in the last 400 years is undoubtedly irregular, with important fluctuations in eruption frequencies, type of eruptions and output rates, both in the long-terms (centuries) and short-terms (decades) [*Hughes et al.,* 1990; *Behncke and Neri,* 2003; *Allard et al.,* 2006].

The period spanning from 1600 to 1669 was characterized by very high output rates (mean of ~1.4 m^3s^{-1}) [*Behncke and Neri,* 2003] and represents the culminating stage of an earlier long cycle lasted several centuries [*Tanguy et al.,* 2003; *Clocchiatti et al.,* 2004].

Since 1669, a new long cycle has started, which is still continuing today. This new long cycle is made up of a first phase (up to mid-1700) characterized by very few, low-fed eruptions (mean effusion rate less than 0.03 m^3s^{-1}), occurred mostly at the volcano summit. Then, a second phase (up to 1865) marked an increase in the mean output rate (~0.2 m^3s^{-1}) and the resumption of a frequent flank eruptive activity (16 events). Flank eruptions and erupted volumes further increased in the third phase (mean output ~0.47 m^3s^{-1}), up to the present [*Wadge et al.,* 1975; *Guest and Murray,* 1979; *Allard et al.,* 2006]. Moreover, short-term eruptive cycles have been observed since 1865 to date, a period during which flank eruptions have occurred in clusters separated by intervals of quiescence and summit activity [*Behncke and Neri,* 2003]. Also these short cycles consist of

three phases: (i) a period of eruptive quiescence lasting less than 3.5 years, (ii) a period of continuous summit activity lasting 6-16 years, and finally (iii) a period marked by flank eruptions alternating with summit activity, lasting 9-22 years. Each short cycle ends with a highly-fed and/or voluminous flank eruption.

An evident increase in the lava output and frequency of eruptions began in 1950, although the behavior remained cyclic [*Allard et al.,* 2006]. Effectively, more than 1.6 km^3 of volume of products have been erupted starting from 1950 at an average rate higher than 0.83 m^{3}s^{-1}. The last short eruptive cycle began after the 1991-1993 flank eruption ($\sim$235 x 10^6 m^3 volume of erupted products), evolving into a couple of years of quiescence, six years of gradually more frequent summit activity, followed by a series of flank (5) and summit (33) eruptions [*Behncke et al.,* 2005; *Allard et al.,* 2006; *Neri et al.,* 2009, 2011a; *Vicari et al.,* 2011b].

Based on numerous and detailed studies conducted on the structural features of flank eruptions at Etna [*Neri et al.,* 2011a, and references therein], the eruptive fissure systems occurring between 1610 and 2012 (Figure 2b-d) were examined. Specifically, a total of 61 flank eruptions were analyzed, which formed 130 segments of eruptive fissures.

During the 17th and 18th centuries, the eruptions generated 22 fissures; 27 eruptive fissures opened during the 19th century, and finally 81 fissures formed during the 20th and 21st centuries. The increasing number of eruptive fissures over time confirms the general increase in frequency of the eruptions.

The length of eruptive systems ranged from a few hundred meters to about 11500 m, with an average of ~3000 meters. About 60% of the eruptive fissures were located above 2400 m altitude; they were mainly radial with respect to the volcano summit, even if most follow a ~N-S trend, namely perpendicular to the direction of regional extension in the area of Etna volcano [*McGuire and Pullen,* 1989; *Lanzafame et al.,* 1996; *Monaco and Tortorici,* 2000; *Solaro et al.,* 2010].

At lower altitude (below 2400 m), the eruptive fissures were clustered in NE, ENE, SE, S and W alignments, following the rift zones. The minimum altitude (~650 m above sea level) of an eruptive vent was reached during the 1669 eruption.

In many cases eruptive fissures do not erupt along their entire lengths (except at the very beginnings of the event); during the propagation of the fissure, the eruptive activity migrates downward and the main vents are commonly located on the lower portions of the fissure itself.

Persistent summit activity during the last 110 years

The summit area of Mt Etna has frequently undergone major morphological changes due to its persistent eruptive activity, both effusive and explosive [*Neri et al.,* 2008].

Four summit craters are active today: the Voragine, the NE Crater, the Bocca Nuova, and the SE Crater (Figure 9). Their eruptive activity consists of: (i) continuous degassing; (ii) mild Strombolian explosions accompanied by slow and poorly-fed (~0.1-1 m^3 s^{-1}) lava effusion from vents inside or on the flanks of the summit craters; and (iii) highly-fed paroxysmal (up to 300-400 m^3 s^{-1}) eruptions, characterized by lava fountains, lava overflows and tephra-rich eruption columns several kilometers high.

This morphological conformation has not always been as it is today. Just 100 years ago there was only one summit crater: the Central Crater (CC) [*Guest*, 1973]. Indeed, during 17th - 18th century, the summit of the volcano had a single deep and wide crater depression, which was formed because of the collapse of the summit area triggered by the huge 1669 eruption [*Corsaro et al.*, 1996]. Later on, during 19th - 20th century, the volcanic activity resumed within this crater, causing its gradual filling.
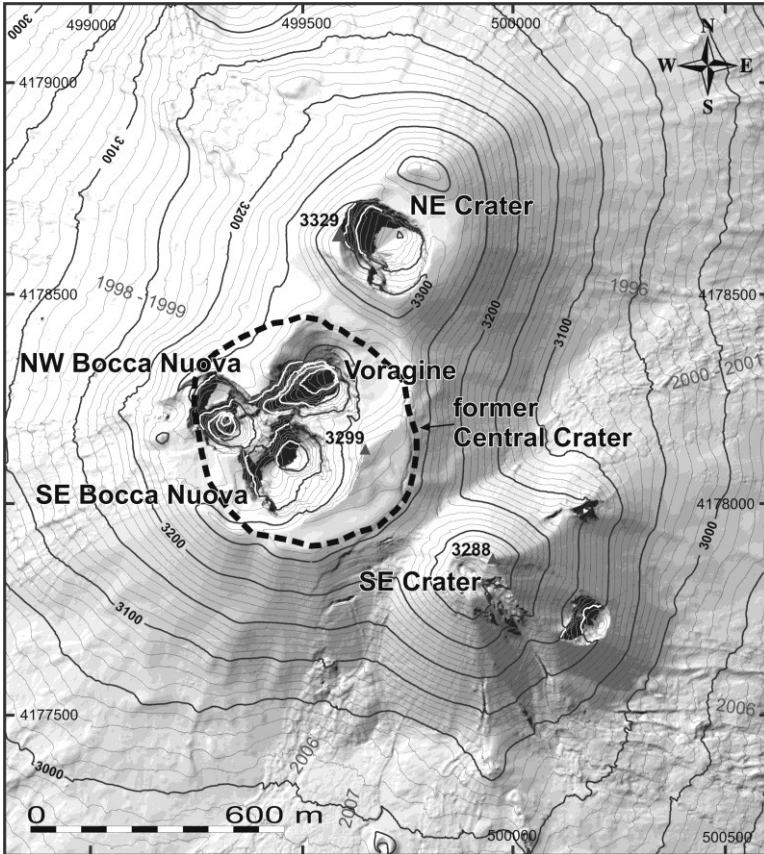
Figure 9 –Topographic map of Etna's summit area carried out in 2007 (from *Neri et al.,* 2008, modified). Equidistance = 10 m. Dashed black line indicates the rim of the former Central Crater mapped in 1932 (Istituto Geografico Militare, 1934). Light grey numbers indicate the age of the main lava flows in the period 1996-2007.

During the almost persistent activity of the Central Crater (CC), the NE Crater (NEC) formed in 1911. At the beginning it was a pit located ~3160m above sea level (a.s.l.) on the northern slope of the CC cone [*Guest*, 1973] and characterized mainly by Strombolian activity. NEC became very active in the second half of the last century, producing numerous and occasionally violent and long eruptions (especially in 1947-1960, 1974-1986, and 1995-1998), up to becoming a major pyroclastic cone as well as the highest point of the volcano (3329.7 m a.s.l. in 2007; *Neri et al.*, 2008).

Starting from the middle of the last century, the CC changed its internal morphology frequently due to the intracrater volcanic activity alternating with subsidence and collapse phenomena. One of these events led to the creation of the Voragine (VOR; also known as "The Chasm") in 1945. VOR formed in the north-eastern portion of the fairly flat floor of CC [*Guest*, 1973]. Major eruptive phases occurred at CC in 1960-1964, which culminated in the opening of eruptive fissures, several paroxysmal events accompanied by huge tephra emissions, continuous lava overflows, and the growth of some pyroclastic intracrater cones [*Behncke et al.,* 2004].

Four years later, in 1968, the Bocca Nuova (BN) was formed still inside the CC, a few tens of meters west of the VOR [*Behncke et al.,* 2003]. The BN widens and deepens gradually, always within the CC,

becoming even larger than the VOR. Later, in 1998, the Strombolian activity resumed at the crater floor, generating several lava fountaining episodes (in 1999) that filled the crater and triggered numerous lava overflows [*Behncke et al.,* 2003; *Calvari et al.,* 2003]. After the 2001 flank eruption, BN and VOR were involved in subsidence, sporadic phreato-magmatic explosions and progressively they collapsed, becoming almost a single crater depression whose edges are, in part, modeled on those of the CC. [*Giammanco et al.,* 2007]. Therefore, it is evident that VOR and BN are internal, minor vents of the CC itself (see dashed black line in Figure 9).

The SE Crater (SEC) formed during the 1971 eruption. Since its origin, SEC has been the most active among the summit craters of the volcano. At first, it was a degassing pit located close to the southeast base of the CC cone, at ~3070 m a.s.l. [*Behncke et al*., 2006]. During the first twenty-five years of activity, SEC erupted quite frequently and built a cone about 100 m high. The cone has grown dramatically in the periods 1996-2001 and 2006-2012, through over 143 paroxysmal episodes and effusive eruptions. Today it has reached an altitude of ~3300 m, forming also a huge new pyroclastic cone on its eastern slope [*Alparone et al.,* 2005; *Behncke et al*., 2006; *Neri et al.,* 2008; *Vicari et al.,* 2011b; *Ganci et al.,* 2012a].

The progressive increase in eruptive activity characterizing the Mt Etna summit area during the last 110 years can be readily seen in Table 1. But what is most striking is the fact that the appearance of the SEC marks a real change in the eruptive frequency. Over the past 41 years, the SEC has produced a number of eruptive events that correspond to more than double the events produced jointly by the CC and NEC in 110 years.

Crater	Paroxysmal episodes	Strombolian activities	Lava flows
Central Crater *(since 1900)*	28	3	16
NE Crater *(since 1911)*	39	10	28
SE Crater *(since 1971)*	154	13	133

Table 1 – Number and type of eruptions per each summit crater. The Central Crater includes the activity of Voragine and Bocca Nuova. The last column (Lava flows) indicates the number of paroxysmal and strombolian events that were also characterized by (i) rheomorphic lavas formed during highly-fed explosive activity; (ii) lava overflows emerging from one of the summit crater; and (iii) lavas erupted from short fissures opened along the external slope of the summit cone (above ~3000 m a.s.l.).

Never in the recent past, has Mt Etna been so active; to find similar levels of activity, we would probably have to go back several hundred years, when the historical chronicles, however, were certainly not as accurate as today.

2.2 Statistical analysis of Etna flank eruptions

Over the last four centuries, the completeness and accuracy of historical data at Mt Etna provides a robust basis for conducting an in-deep statistical analysis to detect spatial and temporal patterns in the distribution of past events, and hence to formulate the appropriate spatiotemporal probabilistic model for the future flank eruptions.

The spatial pattern of eruptive fissures was analyzed using the *Clark and Evans* [1954] index R that measures the ratio between the expected nearest-neighbor distances under complete spatial randomness and the observed mean nearest-neighbor distances:

$$R = \sum_{i=1}^{N} \frac{d_{min}(i)}{N} \bigg/ \left(\frac{1}{2}\sqrt{\frac{A}{N}}\right) \tag{6}$$

where $d_{min}(i)$ is the distance between each eruptive fissure and its nearest neighbor, A is the area of the region, and N is the number of structures considered in the calculation.

In order to consider the eruptive fissures in full, d_{min} is calculated as the "minimax distance", that is the minimum value of the maximum distances between each end point of the i-th eruptive fissure and all the end points of the j-th eruptive fissure [*Cappello et al.,* 2012].

R values less than 1 highlight a cluster tendency, since the observed mean distance between neighboring fissures is less than that expected in random patterns. R equal to 1 points out that casualness is present among data, while R greater than 1 indicates uniformity. The theoretical maximum of R is 2.149 occurring when data are maximally dispersed. With historical data at Etna, an R value equal to 0.027 was obtained, which proves the non-homogeneous spatial distribution of eruptive fissures.

In addition to the spatial analysis, the historical records during the last four centuries were examined to detect the presence of trends or patterns characterizing the temporal distribution of eruption occurrences. It was calculated the cumulative number of eruptive fissure systems linked to flank eruptions over time and the inter-event periods, i.e. the repose times between subsequent eruptions (Figure 10). Both distributions underline the temporal non-stationarity of eruption occurrences, since a growing trend is evident for the number of flank eruptions, while a mainly decreasing tendency stands out for repose times during the last 30 years. This highlights that volcanic

eruptions occurred with a higher frequency in this last period than in the previous ~370 years of activity.
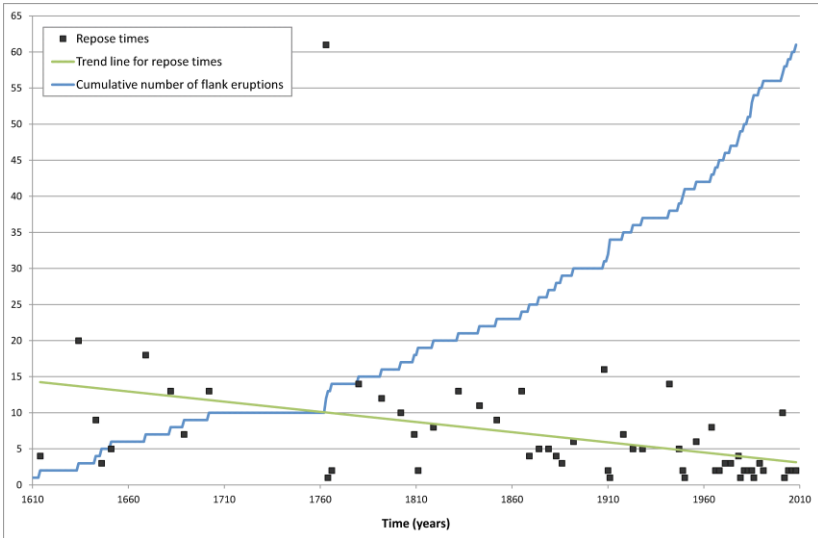

Figure 10 - Cumulative number of eruptive fissure systems opened since 1610 (blue curve). Black dots indicate the repose times in years between the formations of successive eruptive fissures. The straight green line highlights the decreasing trend of repose times, i.e. eruptions occurring more frequently in recent years than in the past centuries.

To evaluate the possible shift over time of the location of the eruptive activity, the centroids of the eruptive fractures in the last 400 years were also calculated, grouping them every 50 years (Figure 11).
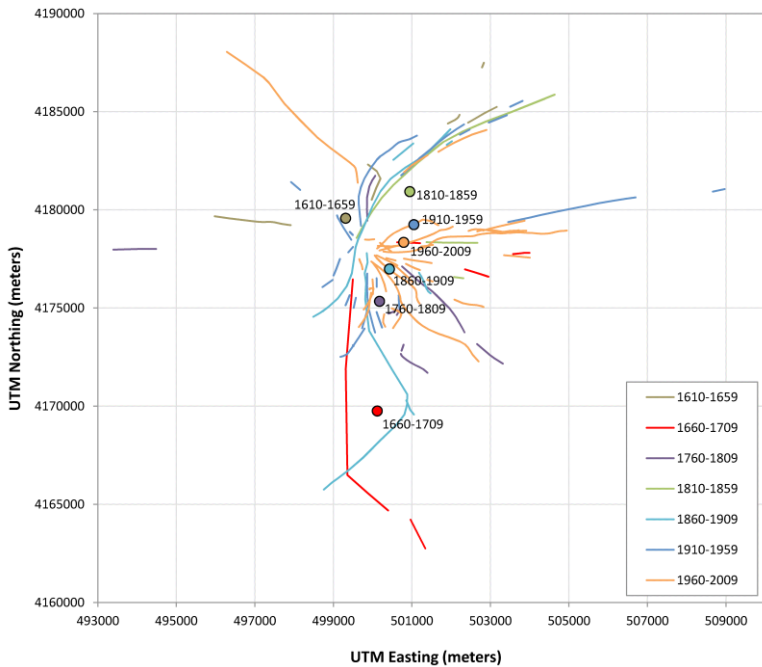
Figure 11 - Centroids of the eruptive fissures opened in the last 400 years, grouped in short periods of 50 years. A spatial shift is evident over time in the location of the eruptive activity, which becomes progressively closer to the summit of the volcano, on the high eastern side. Coordinates are in UTM projection, zone 33N.

The result indicates that the increasing trend in volcanic activity is accompanied by a migration of the centroids that became progressively closer to the summit of the volcano, on the high eastern side. This fact is testified by the rapid morpho-structural evolution of

the summit area during the last decades: the former Central Crater (the single summit crater existing up to early 1900) was modified by the growth of the NE Crater (formed in 1911 on the northern side), the Bocca Nuova (formed in 1968 inside the Central Crater and close to the its western rim) and the SE Crater (formed in 1971 on the southeastern side), which represent the connections of the three main volcanic rifts in the summit area [*Neri et al.,* 2011].

The in-deep analysis conducted on flank eruptions in the last four centuries demonstrates the spatial non-homogeneity and the temporal non-stationarity of flank activity, hence suggesting that the most appropriate space-time probabilistic model for the future flank eruptions at Etna volcano is a non-homogenous Poisson process (NHPP) with a time-varying intensity function.

2.3 The space-time probabilistic modeling of flank eruptions

The first and maybe most important step in forecasting lava flow hazards involves the construction of a spatiotemporal probability map for the identification of the most probable emission zones of future lava flows.

In order to accurately assess the distribution of future vent opening, the methodology for building the probability map should include the

analysis of the spatial location of past eruptive events, as well as the eruption frequency within a time window. At Etna, the probabilistic modeling was based on the locations of the pre-1600 eruptive fissures, dykes and faults (for which an exact dating cannot be established), and on the spatial positioning and temporal sequencing of the post-1600 flank eruptions occurred at Etna (that are accurately documented and well-dated).

Over the same grid of potential vents $v_i(x,y)$ defined in Figure 5, separate PDFs were calculated using the formula of the Gaussian kernel:

$$\lambda_{xyt} = \sum_{i=1}^{N} \left(e^{-\frac{d_i^2}{2h^2}} * e^{kt_i} \right) \qquad (7)$$

where N is the total number of volcanic structure considered in the calculation, d_i is the distance between the potential vent $v_i(x,y)$ and the i-th volcanic structure, t_i is the elapsed time since the eruption at the i-th eruptive fissure, h is the smoothing factor, and k is a constant. The smoothing factor h determines the intensity of influence of each volcanic structure, giving them high emphasis (for small values of h) or yielding a more uniform distribution across the area (for large values of h). The h smoothing factors used in Equation 7 are the same

obtained with the LSCV: 1000 m for the post-1600 fissures, 1200 m for the pre-1600 fissures, 1050 m for the dykes and 1350 m for the faults [*Cappello et al.,* 2012].

The constant k serves the purpose of assigning larger weights to more recent events with respect to older ones. For the pre-1600 eruptive fissures, dykes and faults, k has the value of zero since an exact date t_i for these ancient volcanic structures cannot be established. For the post-1600 fissures, the best fit for the constant k was estimated using the back analysis approach described in Paragraph 1.2 to quantify how the distribution of the oldest eruptive fissures has affected the formation of the most recent ones.

Specifically, the best fit for the constant k was retrieved by evaluating the mean square error of each probability forecast with the Brier score [*Brier*, 1950]:

$$BS = \frac{1}{N}\sum_{i=1}^{N}(p_i - o_i)^2 \qquad (8)$$

where p_i is the forecast probability of each grid cell and o_i indicates whether an eruptive fissure has been formed in that cell after 1981 ($o_i = 1$ if at least a fissure has occurred and $o_i = 0$ if not).

The Brier score runs from 0 to 1, with smaller values indicating better forecasts. The value for k which minimizes BS was found to be -0.00107 and used it in Equation 7 for all post-1600 eruptive fissures. The PDFs for pre-1600, post-1600 eruptive fissures, dykes and faults, after being normalized so that their integral across the whole area is unity, were aggregated in a linear combination $Λ_{xyt}$ using the weights calculated with Equation 5 (0.15, 0.6, 0.15 and 0.1, respectively, for pre-1600, post-1600 eruptive fissures, dykes and faults).

In order to consider the variability of the flank volcanic activity over time, the year of formation of each eruptive fissure opened since 1610 was used to calculate the temporal intensity with the power intensity function [*Ho,* 1991; *Smerthust et al.,* 2009]:

$$\lambda(t) = \frac{\delta}{\theta}\left(\frac{t-T_1}{\theta}\right)^{\delta-1} \quad for \ t \geq T_1 \tag{9}$$

where T_1 is the year of the oldest eruptive fissure, t is the year of interest, and δ and θ are unknown positive parameters. The parameter δ determines the shape of the power function: $\delta>1$ (resp. $\delta<1$) corresponds to an increasing (resp. decreasing) intensity with time, while $\delta=1$ reduces Equation 9 to a homogenous process.

The best estimates of δ and θ (Table 2) are found by minimizing the square differences of residuals between the expected amount (computed as the integral of λ from T_1 to t) and the actual number of eruptions over time (estimated as the cumulative number of events observed up to t) on the entire catalogue (from $T_1=1610$ to $T_2 = 2012$; see Figure 12a). In order to indicate the reliability of the estimates of δ and θ, the 95% confidence intervals are also listed (Min and Max estimates in Table 2).

Parameters	Min estimates	Best estimates	Max estimates
δ	1.555	1.596	1.636
θ	34.843	32.932	31.022
$\lambda(T_2+1)$	0.174	0.216	0.270
$\lambda(T_2+10)$	0.176	0.219	0.274
$\lambda(T_2+50)$	0.185	0.231	0.291

Table 2 – Estimates of the parameters δ and θ calculated by minimizing the square differences of residuals between the expected and actual number of eruptions over time (Best estimates), with the 95% confidence intervals (min and max estimates). The evaluations of δ and θ are then used to calculate the recurrence rate $\lambda(T_2+p)$ with $T_2 = 2012$ and $p = 1, 10, 50$.
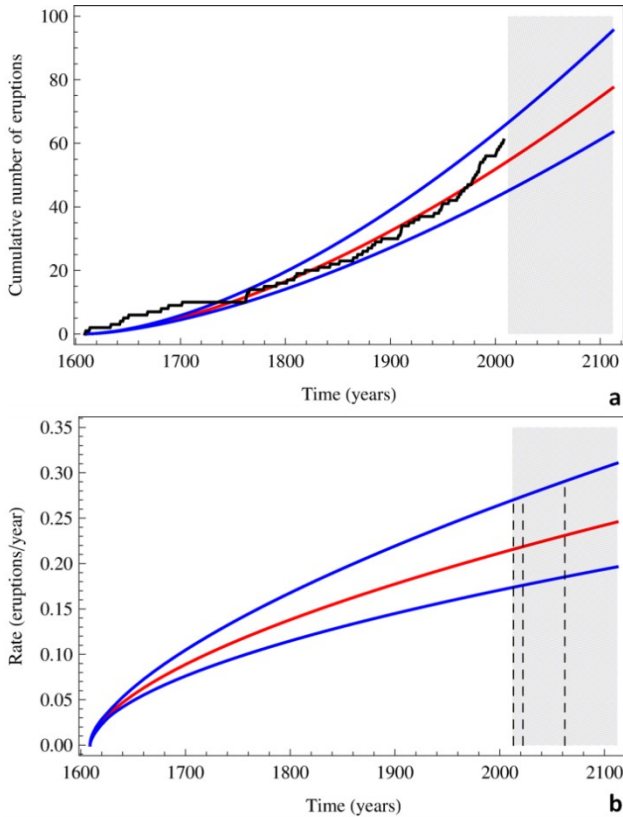
Figure 12 - (a) Actual cumulative number of eruptions (black curve); best estimate calculated by minimizing the square differences of residuals between the expected and actual number of eruptions over time (red curve); and the 95% confidence interval (blue curves) of the best estimate. (b) The corresponding power intensity functions $\lambda(t)$. The future rates (listed in detail in Table 2) are obtained by extending the curves for the different forecasting periods highlighted by the dashed lines over the gray bar, i.e. the coming year and the next 10 and 50 years.

Using the obtained values of δ and θ, the curves of annual recurrence rates were extrapolated for different forecasting periods p (1, 10 or 50 years), and the minimum, best and maximum temporal intensities were calculated with Equation 9 for $t = T_2 + p$ (Figure 12b).

The best recurrence rate for the next 50 years (0.231; see Table 2) was employed to rescale the linear combination of the four PDFs Λ_{xyt}, which was used to calculate the final spatiotemporal probability map for future opening:

$$p_a(v_i, \Delta t) = 1 - e^{-\Lambda_{xyt}\Delta x \Delta y \Delta t} \qquad (10)$$

Thereby p_a specifies the probability of activation of each potential vent $v_i(x, y)$, i.e. the probability that at least one eruption will occur in the unit area $\Delta x \Delta y$ (500 m × 500 m) within the considered Δt (50 years) time period.

2.4 Results

The final resulting map showing the spatiotemporal probability of future vent opening in the next 50 years is displayed in Figure 13.
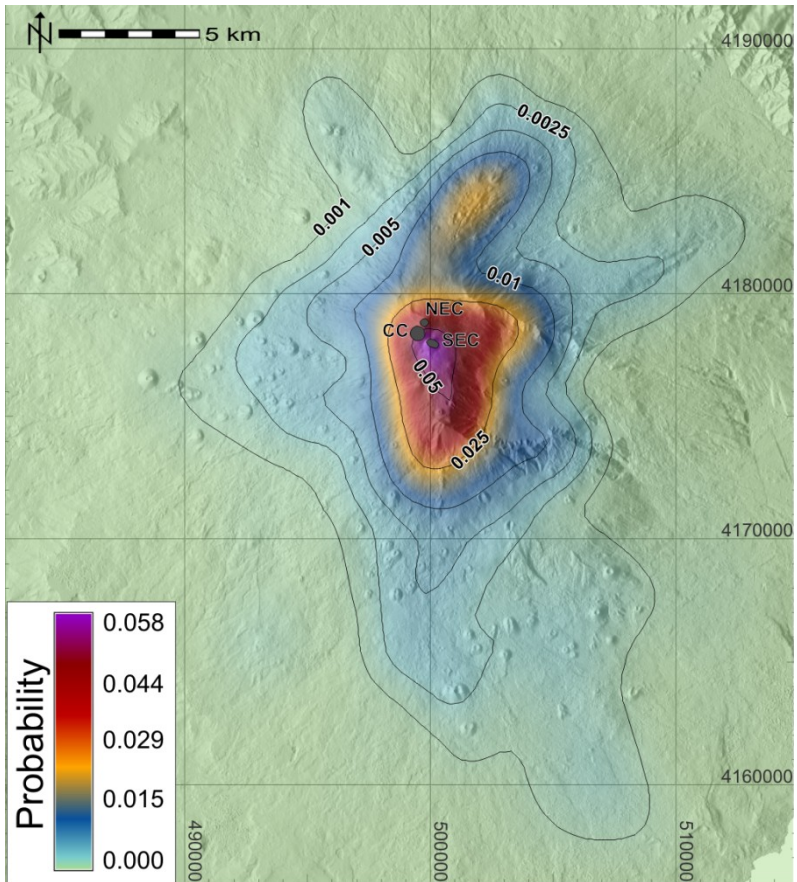
Figure 13 – Spatiotemporal probability map of vent opening in the next 50 years, calculated combining the temporal and spatial analysis of Etna flank eruptions. Summit craters are masked because their activity was separately investigated.

Two results leap out in Figure 13 with respect to the susceptibility map of Figure 8:

- The probability of vent opening is assigned higher estimates overall. In particular, the highest value reached is 0.058, which is one order of magnitude higher than the maximum value found for the susceptibility map (0.004). This outcome is correctly reflects the increase in eruption frequency beginning in 1950 that was not considered in the exclusive spatial analysis;

- The distribution of probabilities tends to become less homogeneous, showing a high concentration around the summit area. This result is motivated by the morpho-structural evolution of the summit area of the last decades due to the growth of the NE Crater (in 1911), the Bocca Nuova (in 1968) and the SE Crater (in 1971).

Clearly the resulting map does not represent a deterministic forecast of the future eruptions, but a prediction originated from a statistical probabilistic analysis of the eruptive activity of Etna.

2.5 Statistical modeling of summit eruptions

The persistent summit activity documented at Etna from the first decades of the 20th Century until today represents a good source for

a statistical analysis. Thus a more comprehensive and accurate study in forecasting volcanic eruptions was provided estimating also the space-time annual rate of eruptive events at the summit craters (Figure 9): the CC (comprising VOR and BN), the NEC and the SEC (including the new cone recently formed on its eastern slope).

The dataset for the statistical analysis comprises the various types of eruptions occurring since 1900 at the summit craters of Etna, including paroxysmal episodes and Strombolian activities (see Table 1). Two kinds of analysis were conducted on this dataset. First the recurrence rate of the summit activity was calculated considering the whole catalogue of eruptions. Next the datasets were divided in three samples and space-time forecasts were estimated for each summit crater (CC, NEC and SEC).

For the recurrence rate of the summit activity as a whole, the best values for the parameters δ and θ (Table 3) were estimated minimizing the square differences of residuals between the expected and the actual number of eruptions over time (Figure 14a). These best estimates were then used in the power intensity function described by Equation 9 to obtain the curves of recurrence rates with the expected number of eruptions for the next 1 and 10 years (Figure 14b). Unlike the analysis of flank eruptions, forecasting periods longer than 10 years were not used since they might provide inconsistent results

starting from the short time series of documented summit eruptions (~110 years).

Parameters	Min estimates	Best estimates	Max estimates
δ	4.570	4.893	5.217
θ	38.719	36.197	33.676
$\lambda(T_2+1)$	5.402	12.327	25.530
$\lambda(T_2+10)$	7.102	17.030	35.268

Table 3 – Estimates of the best values for δ and θ (Best estimates) and the 95% confidence intervals (Min and Max estimates), and the relative recurrence rates $\lambda(T_2+p)$ with $T_2 = 2012$ and forecasting periods $p = 1, 10$ years. The estimates are calculated considering the activity of summit craters as a whole.

The best values of recurrence rates for the coming year (12.327) and the next 10 years (17.030) estimate that slightly more than one eruption per month is expected in the entire summit area. In the worst cases, more than two (25.530) and about three eruptions (35.268) per month could occur, respectively, in the next 1 and 10 years. These estimates are strongly influenced by the extraordinary activity that took place at SEC in 2000 (66 short-term lava fountains) and recently between 2011 and 2012 (25 mid-term lava fountains).
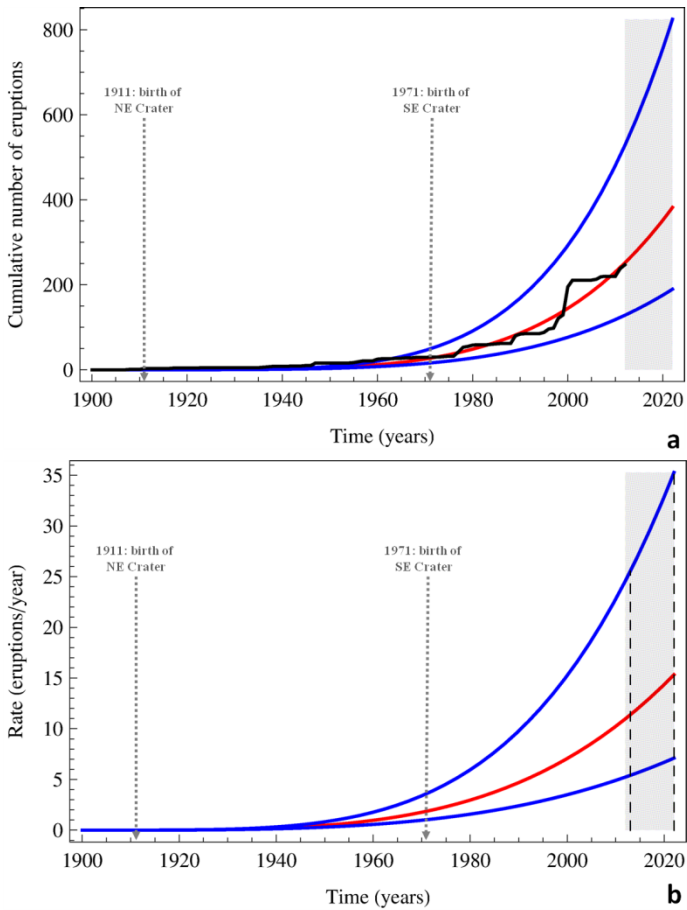
Figure 14 – Actual cumulative number of eruptions (black curve) compared with the best estimate (red curve) and its 95% confidence interval (blue curves). The formations of the NE Crater in 1911 and of the SE Crater in 1971 are highlighted. (b) Power intensity functions λ(t) calculated with the temporal rates for the next 1 and 10 years reported in Table 3.

For the space-time forecast, the catalogue was divided in three datasets selecting the eruptions occurring at CC, NEC, and SEC. With these three datasets the best expected numbers of eruptions were calculated (Figure 15a-c), from which the best estimates for parameters δ and θ (Table 4) were derived. The recurrence rates were estimated for the coming year and the next 10 years (Figure 15d-f).

Parameters	Central Crater	NE Crater	SE Crater
δ	1.541	2.240	2.650
θ	11.997	16.495	5.832
$\lambda(T_2+1)$	0.461	1.453	14.582
$\lambda(T_2+10)$	0.484	1.641	22.010

Table 4 – Best values for δ and θ, and the relative recurrence rates $\lambda(T_2+p)$ with $T_2 = 2012$ and forecasting periods $p = 1$, 10 years. The estimates are calculated considering the activity of the Central Crater (since 1900), of the NE Crater (since 1911), and of the SE Crater (since 1971), separately.

The spatio-temporal analysis suggests that the expected number of eruptions at the CC (from 0.461 to 0.484) is comparable with the rates obtained for the flank eruptions (from 0.216 to 0.219). Unlike those of the NEC and of the SEC, the curve of the annual rate for the

CC shows a decreasing speed of growth. At the NEC the expected number of eruptions augments uniformly, reaching an annual rate of 1.453 and 1.641, respectively, for the next 1 and 10 years. But the summit crater showing the most exceptional activity is undoubtedly at the SEC. On the basis of the historical eruptions since its formation in 1971, we expected a number of eruptions equal to 14.582 for the coming year, that is more than one eruption per month, and 22.010 eruptions in the next 10 years, namely slightly less than two events per month.
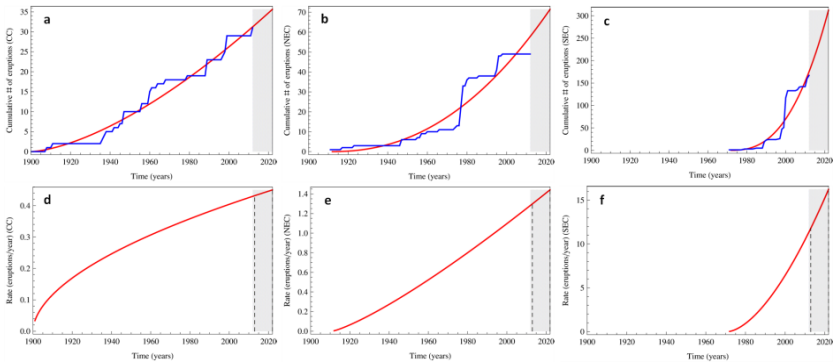

Figure 15 –Actual (blue curve) and modeled (red curve) cumulative number of eruptions for the (a) Central Crater (CC), (b) the NE Crater (NCE), and (c) the SE Crater (SEC). The power intensity functions calculated with the best rates for the next 1 and 10 years are also shown respectively for CC (d), NEC (e), and SEC (f).

Chapter 3

Characterization of expected eruptions

Forecasting the lava flow hazard requires an extensive effort to characterize consistent classes of expected eruptions for calculating the local probabilities of occurrence for each class and deducing essential input information for the lava flow simulations.

The characterization of expected eruptions exploits the knowledge of the effusive activity data at Mt Etna referring to the past 400 years, from 1607 to 2006.

Data were extracted from [*Proietti et al.,* 2011]:

- Three geological maps: the New Geological Map of Etna volcano, which was updated to 2007 [*Branca et al.,* 2011], and the previous ones compiled by *Waltershausen* [1845-59] and *Romano et al.* [1979];

- Orthophotos extracted from aerial surveys in 1994, 2001 [Coltelli et al., 2007], 2004 [Baldi et al., 2006] and 2005 [Gwinner et al., 2006];

- Lava flow maps reported in Azzaro and Neri [1992].

For each lava flow field, different information were collected, including the eruption year, the eruption style, duration, the invaded area, the lava volume emitted and the main vent, which is defined as the single vent associated to the main lava flow of each effusive eruption.

Although sixty-six lava flows were identified on the base of effective outcropping flow areas [Proietti et al., 2011], ten effusive events were excluded due to the incompleteness of records in one or more fields. In particular, five lava fields cannot be located: four (1643, 1702, 1755 and 1918) do not outcrop in any of the maps and one (1975) cannot be distinguished from another flow field (1975-77) occurred shortly afterwards in the same area. Other three events (1956, 1964 and 1975-77) were also kept out because of unknown

volumes, and two (1682 and 1689) for unknown durations and volumes.

All fifty-six remaining eruptive events were analysed, although some of them exhibit an extraordinarily brief (1869, 1908 and 1942) or long (1651-54 and 1614-24) duration, as well as extremely low (1883, 1968, and December 1985) or high (1651-54 and 1669) lava volumes.

Among these events, the 1669 eruption (11 March to 11 July) is absolutely unique due to the low altitude of the vents (~800 m a.s.l.) and the large volume of lava erupted (~1000×10^6 m^3) that induced the lava flow branches to run over long distances, flooding a fairly densely populated area and threatening several towns and villages [*Corsaro et al.,* 1996], including Catania, which was partly destroyed.

An artistic representation of the 1669 eruption is exhibited in the Cathedral of Catania (Figure 16). It is an impressive fresco of Giacinto Platania, one of the greatest Sicilian painters and decorators of the XVII Century, who came to Catania to follow the development of the dreadful event.

Figure 16 – The fresco painting of Giuseppe Platania exhibited in the sacristy of the Cathedral of Catania, documenting the destructive invasion by lava flow during the 1669 Etna eruption.

3.1 Definition of the expected eruptive classes

For the statistical analysis, the information about duration and lava volume were cross-checked. On the base of the distribution obtained, a time barrier (at 30 days) was fixed for the duration and two volume barriers (at 30 and 100×10^6 m^3) were set for the lava volume emitted.

In this way six eruptive classes were inferred, five of which are populated (Figure 17).

Although an eruptive event characterized by duration less than 30 days and a lava volume of more than 100×10^6 m^3 is not occurred in the last four centuries of Etna activity, it was maintained as an extreme event and a probability of occurrence close to zero was assigned to the correspondent eruptive class.
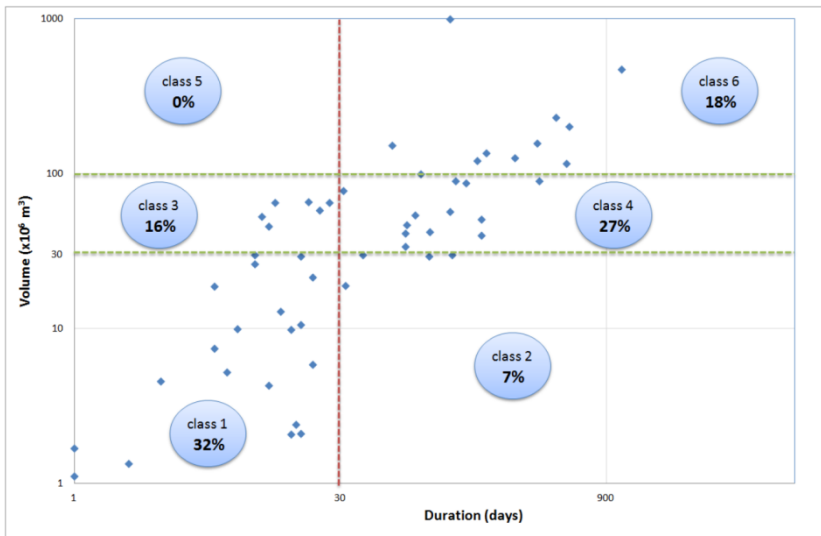

Figure 17 – The six eruptive classes obtained analyzing duration and lava volume of eruptions occurred at Etna volcano since 1607. The red line suggests the time barrier (30 days) for the duration, while the two green lines show the volume barriers for the lava volume (30 and 100×10^6 m^3). The percentages of occurrence for each eruptive class are also reported.

3.2 Occurrence probability for each eruptive class

The probability that one of the six classes may occur in future was evaluated applying the Gaussian kernel to each potential vent $v_i(x,y)$ of the grid (see Figure 5).

First the main vents were divided per eruptive class and their locations (Figure 18) were used to estimate the smoothing parameters h minimizing the LSCV (Equation 4).
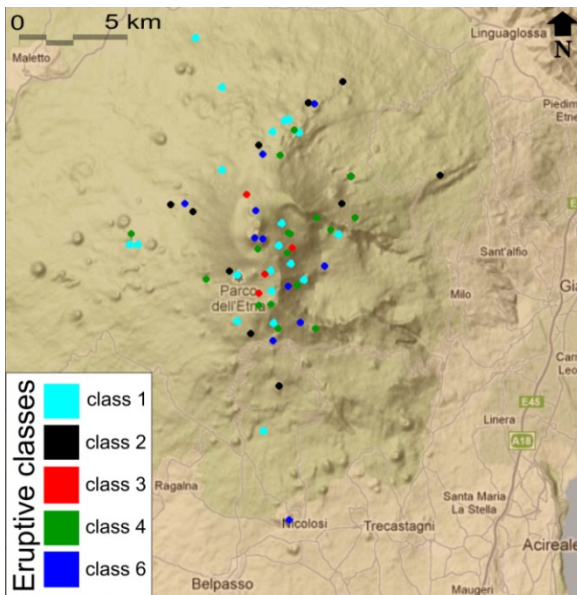

Figure 18 – Main vents divided in the six eruptive classes defined on the base of the duration and the volume of lava erupted.

For each eruptive class the following values of h were obtained: 3200 m for class 1, 4000 m for class 2, 6700 m for class 3, 2900 m for class 4 and 4100 m for class 6.

Then the formula of the Gaussian kernel for point patters was used to calculate the spatial density in each potential vent $v_i(x,y)$:

$$p_e(v_i) = \frac{1}{2\pi h_e^2 N_e} \sum_{j=1}^{N_e} e^{-\frac{1}{2}\left[\left(\frac{x-x_j}{h}\right)^2 + \left(\frac{y-y_j}{h}\right)^2\right]} \tag{11}$$

where x_j and y_j are the Cartesian coordinates of the main vents belonging to the class e, and N_e is the cardinality of e.

Obviously, Equation 11 can be applied only to the events of classes 1, 2, 3, 4 and 6, which are then rescaled so that the integral across the area equals the percentages of occurrence per class reported in Figure 17. Conversely, for the eruptive class 5 that is empty, an extremely low homogenous density was defined so that the integral across the area has a probability close to zero (0.0001).

Finally, for each potential vent $v_i(x,y)$, the estimates p_e are rescaled so that:

$$\sum_{e=1}^{6} p_e(v_i) = 1 \tag{12}$$

Chapter 4

Numerical simulations of lava flow paths

Mathematical models simulating the evolution of volcanic phenomena allow the estimation of the area affected by an eruptive event and accounts for the influence of the actual topography on the path of future lava flows [*Pareschi et al.,* 2000]. Hence the estimation of the hazard with the aid of the simulation approach provides a more robust and locally accurate analysis than a simple probabilistic approach.

This Chapter describes the MAGFLOW model, representing the central part of the methodology for the hazard assessment of lava flow inundation.

On Etna, MAGFLOW has been successfully used to reproduce lava flow paths during effusive eruptions [*Vicari et al.,* 2007; 2009; *Del Negro et al.,* 2008; *Hérault et al.,* 2009; *Ganci et al.,* 2012b] and paroxysmal events [*Vicari et al.,* 2011b]. More recently, it has been applied to consider the impact of hypothetical protective barrier placement on lava flow diversion [*Scifoni et al.,* 2010], and to produce the lava flow invasion hazard map at the South-East Crater [*Vicari et al.,* 2011b].

4.1 The MAGFLOW model

MAGFLOW is a physics-based model for lava flow simulations based on a Cellular Automaton (CA) approach developed at INGV-Catania [*Vicari et al.,* 2007, *Del Negro et al.,* 2008].

The MAGFLOW simulation domain is decomposed into square cells whose width matches the resolution of the Digital Elevation Model (DEM) available for the area. The computational domain of a simulation is chosen large enough to include the prospected maximum extent of the lava flow emplacement. The ground elevation provided by the DEM, the fluid lava thickness, the solidified lava thickness, the heat quantity, the temperature, and the amount of solidified lava are the five scalar quantities carried by each cell.

The evolution of the system is purely local, in the sense that each cell evolves according to its present status and the status of its Moore neighborhood (i.e. its eight immediate neighbors). Lava thickness varies according to lava influx from the vent for cells corresponding to a vent location, plus any lava flux between neighboring cells. Cross-cell lava flux is derived from a steady-state solution for the Navier-Stokes equations for a fluid flowing on an inclined plane with Bingham rheology [*Dragoni et al.,* 1986]. The approximation coming from the use of a steady-state solution is justified by the high viscosity of lava flows.

The rheological parameters are the yield strength S_y and the plastic viscosity η. The Bingham flow condition, requiring that shear stress is higher than the yield strength, is modeled by introducing a critical height h_{cr} and having flux between two adjacent cells only when h is greater than h_{cr}, with h being the lava height in the cell with higher total height. The volumetric flux q is therefore zero if 800 K, and is otherwise given by

$$q = \frac{S_y h_{cr}^2 \Delta x}{3\eta} \left(a^3 - \frac{3}{2} a^2 + \frac{1}{2} \right) \tag{13}$$

where Δx is the distance between adjacent cells, and a $= h/h_{cr} > 1$.

The critical thickness h_{cr} is computed from the yield strength and slope angle to account for both pressure and gravity-driven flows:

$$h_{cr} = \frac{S_y}{\rho g(\sin\alpha - \vartheta h/\vartheta x \cos\alpha)} \cong S_y \frac{\sqrt{\Delta z^2 + \Delta x^2}}{\rho g(\Delta z + \Delta h)} \tag{14}$$

where ρ is the lava density, α is the slope angle of the inclined plane, g the gravity acceleration, Δz the overall solid height difference (considering ground elevation and solid lava height), and Δh the difference in lava thickness, as computed at the cell with highest total height (Figure 19).
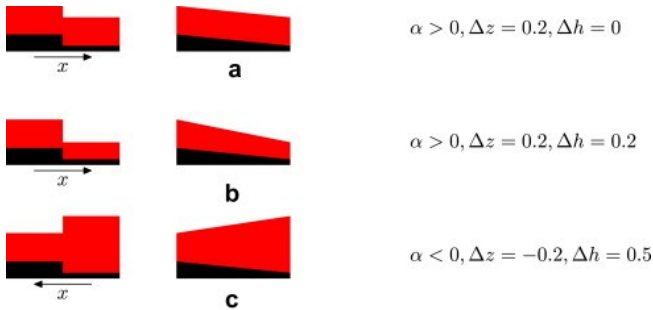

Figure 19 – Local reference system for computing the critical height. The discrete formula is found from the approximations $\sin\alpha = \Delta z/\sqrt{\Delta z^2 + \Delta z^2}$, $\cos\alpha = \Delta x/\sqrt{\Delta z^2 + \Delta z^2}$, $\partial h/\partial x = -\Delta h/\Delta x$ with Δz and Δh computed from the cell with higher total height. Case (a): pure slope-driven flow; case (b) slope- and gravity-driven flow; case (c): gravity-driven flow in direction opposite to slope.

Following *Ishihara et al.* [1990], the yield strength is computed according to the formula

$$log_{10}S_y = 13.00997 - 0.0089T \tag{15}$$

and the viscosity follows *Giordano and Dingwell* [2003]

$$log_{10}\eta = -4.643 + \frac{5812.44 - 427.04 \times H_2O}{T - 499.31 + 28.74 \ln(H_2O)} \tag{16}$$

with T being the temperature in Kelvin and H_2O the water content in weight percent (wt %). MAGFLOW assumes constant (average) water content across the flow, and its value is a user-controlled parameter typically in the range 0.02 - 0.2 wt %.

The actual amount of lava gained or lost by a cell at each iteration is given by the total flux Q of the cell multiplied by the timestep Δt for that iteration.

To prevent non-physical solutions, the timestep is controlled by ensuring that for each cell

$$Q\Delta t < chA \tag{17}$$

where h is the lava height in the cell and A the cell area. The constant $0 < c < 1$ ensures that only a fraction of the total fluid lava volume is lost at each iteration, and should be selected small enough to ensure that the stationary solution of the Navier-Stokes equation used to compute the flux remains approximately valid during the next step. The timestep used by the CA is then the minimum of the Δt computed by each cell according to the inequality (17).

Cells are considered at constant temperature (no vertical temperature gradient), and heat flux is computed from mass flux considering the temperature of the cell losing mass. Heat loss is only considered with radiation from the surface, ignoring the effects of conduction to the ground and convection in the atmosphere.

Solidification follows a simplified model that does not take into consideration phenomena such as plug or crust formation. When the temperature of a cell drops below a given solidus temperature T_s, defined as the temperature below which lava stops flowing, a corresponding fraction of the lava in it is converted to solid lava, which is assumed to lie at the bottom of the cell, thereby contributing to the total height of the cell but not to the amount of fluid that can move.

To produce a dynamic picture of probable lava flow paths, MAGFLOW requires constraint of many parameters. These include:

(i) a knowledge of the chemical composition of the lava (this places constraints on the eruption temperature of the lava, the relationships between lava temperature and viscosity, and temperature and yield strength, all of which are used to compute the rate at which the lava solidifies), (ii) a digital representation of the topography over which the lava is to be emplaced, (iii) the location of the eruptive vents, and (iv) an estimate of the lava discharge rate.

4.2   Sensitivity analysis of the MAGLOW input parameters

The sensitivity analysis (SA) of MAGFLOW [*Bilotta et al.,* 2012] is focused on the rheological and physical parameters which are currently measured during eruptive events, namely water contents and eruptive and solidus temperature.

The purpose is to assess the impact that measurement errors have on the results of the simulation and therefore to identify the critical parameters, information which is important in applications to scenario forecasting during eruptive events, and to provide suggestions for more research in modeling.

There are a number of other possible parameters that could be taken into consideration for the SA. For example, the coefficients that appear in the yield strength Equation (16), or the ones controlling the

viscosity law (Equation 17), are derived from experimental data, and it would be useful to determine to what degree they influence the simulations.

However, the extreme computational complexity of evaluating the impact of all these parameters led to restrict the selection to the ones on which data is more likely to be available on a short notice during eruptive events.

Methodology

An initial attempt to the SA of MAGFLOW's parameters was based on Affine Arithmetic (AA) [*de Figueiredo and Stolfi,* 2004], to exploit its capability of correlating the final results with the uncertainty in the input parameter, a significant advantage during the analysis of the influence of multiple parameters.

However, the high non-linearity of the numerical operations quickly cancels the benefits of the use of AA: most of the data in the result loses most of its correlation to the prescribed uncertainty in the parameters after a few iterations of the automaton, and since most simulations run for thousands of iterations, the final results contain overestimated, uncorrelated uncertainties which give little insight on the parameter dependency. Moreover, the discrete nature of the

evolutionary processes of the CA substantially increases the computational complexity, which makes the application of AA, or any other self-verified numerical method, too complicated for practical use in this case.

In the case of cellular automata, commonly used approaches to sensitivity analysis are focused on the specific nature of cellular automata, and analyze the topological influence of properties such as cell size and shape or neighborhood structure and width [*Kocabas and Dragicevic,* 2006; *Moreno et al.,* 2008]. However, the focus of the MAGFLOW sensitivity analysis is instead on the rheological and physical parameters driving the cellular automaton evolution function.

The actual SA has therefore been completed with a more specific and effective approach based on the recent development of the use of polynomial chaos expansion (PCE) for uncertainty quantification [*Sudret,* 2008; *Crestaux et al.,* 2009]. In this context, polynomial chaos expansion can be used to determine the Sobol' sensitivity indices, and therefore quantify the impact that each parameter has on the variance of a given function.

As for the applications of the MAGFLOW model (scenario forecasting, hazard evaluation), the lava flow emplacement, i.e. the area subject to invasion by the flow, is most important morphological

aspect. The difference in emplacement between distinct lava flow fields (actual or simulated) can be quantified by a single scalar value with a fitness value, computed as the ratio between the intersection and the union of the affected areas (Figure 20).
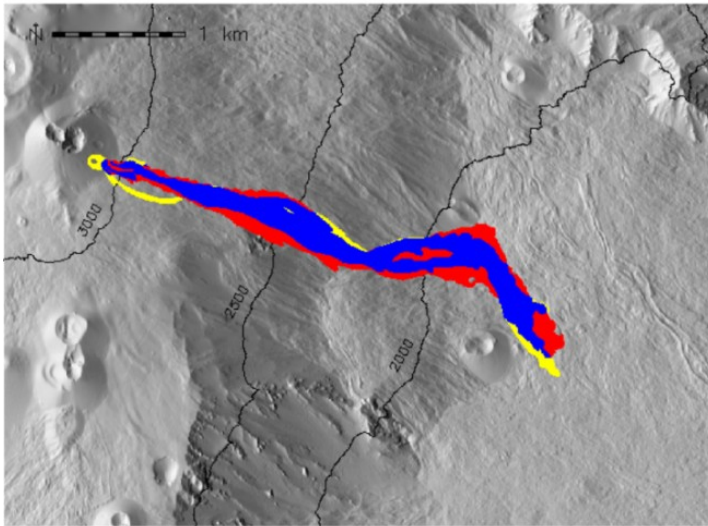

Figure 20 – Graphical representation of fitness computation obtained overlaying a test simulation with an actual emplacement (reference). Blue (0.58 km^2) denotes common invasion areas, yellow (0.08 km^2) denotes underestimated areas (in the reference but not in the tested simulation), red (0.03 km^2) denotes overestimated areas (in the tested simulation but not in the reference). Fitness is computed as the ratio between the blue area and the union of all the areas, and in this case would be $\Phi = 0.58/(0.58+0.08+0.03)$ =0.8406 (e_1=0.9168).

In formulas, for any emplacement A let |A| be the measure of its area, and for any two emplacements A and B, let $A \cup B, A \cap B$ denote as usual the union and intersections of the respective areas. Then the fitness function is given by

$$\Phi(A,B) = \frac{|A \cap B|}{|A \cup B|} \tag{18}$$

This fitness function is the same used e.g. by *Favalli et al.* [2009a] in the sensitivity analysis of the DOWNFLOW probabilistic model for lava flow simulation.

Other choices of fitness functions are also possible; for example, *Rongo et al.* [2008] define a fitness function $e_1 = \sqrt{\Phi}$ to evaluate the application of the SCIARA cellular automata model for lava flows.

The behavior of Φ and e_1, and therefore the preference of one over the other, is largely dependent on the shape of the emplacement.

Assume that the reference emplacement is a perfect circle of radius R (ideal case of eruption from circular vent on a horizontal plane), with the test simulation being a concentric perfect circle of radius r. Thus $\Phi = r^2/R^2$, while $e_1 = r/R$ with e_1 seemingly more appropriate than Φ. By contrast, for a channel flow of reference length L, test

simulations of length l have $\Phi = l/L$ and $e_1 = \sqrt{l/L}$, and Φ would seem more appropriate than e_1 as a fitness index.

For the SA of the MAGFLOW rheological parameters, values for both Φ and e_1 have been provided, to ease comparisons with the other lava flow models mentioned earlier. While the specific quantitative values of the fitness evaluations in the sensitivity analysis depend on the choice of fitness function, the qualitative behavior of the parameters will be the same for both choices, as illustrated by the overall sensitivity indices.

The tests for the SA were built with the following possible ranges of the parameters considered:

- water percentage H_2O; range: 0.02 wt % - 0.2 wt %;
- solidus temperature T_s; range: 800 K - 1100 K;
- eruption temperature T_e; range from 1360 K - 1450 K;

The range of variations were chosen based on the current geophysical knowledge about the properties of Etnean lavas, as well as from the results of the calibration and validation tests run during the development of the MAGFLOW model.

Due to the wide amplitude of its range (one order of magnitude), the logarithm of the water percentage parameter was considered as raw parameter in the SA, rather than the water percentage itself.

The DEM and the flux rates for all simulations were taken from the available data for the 2006 eruption [*Vicari et al.,* 2009]. Since the aim was not validation but sensitivity analysis of MAGFLOW, the reference eruption for the fitness function was the simulation with the midpoint values H_2O = 0.06325 wt%, T_s = 950 K, T_e = 1405 K, rather than the actual lava flow extent of the 2006 eruption.

Results

As a preliminary to the results of the SA, fitness variation plots for the three parameters when considered independently are reported. Results (Figures 21-23) give a qualitative idea of the influence that each parameter has on the simulation, independently of the others.
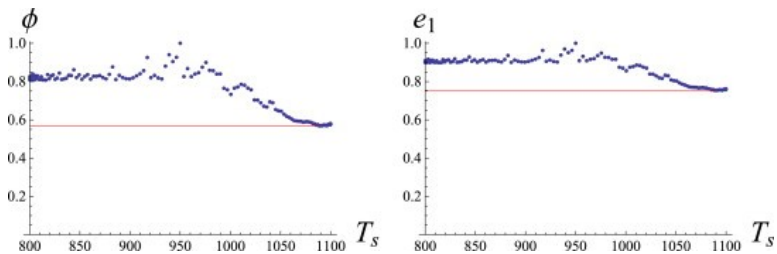

Figure 21 – Fitness variation for the solidus temperature, assuming fixed average values for the water percentage and eruption temperature. The red line marks the lowest value achieved.
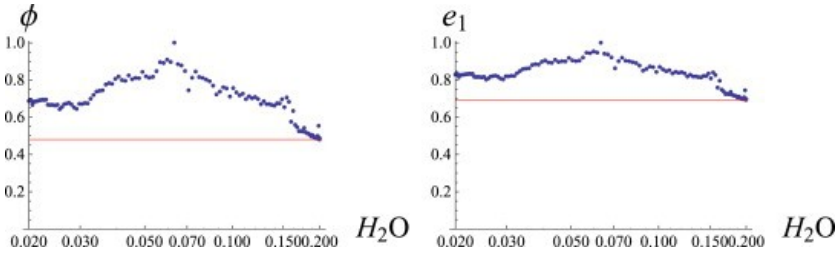
Figure 22 – Linear-log plot of fitness variation for the water content, assuming fixed average values for the solidus and eruption temperature. The red line marks the lowest value achieved.
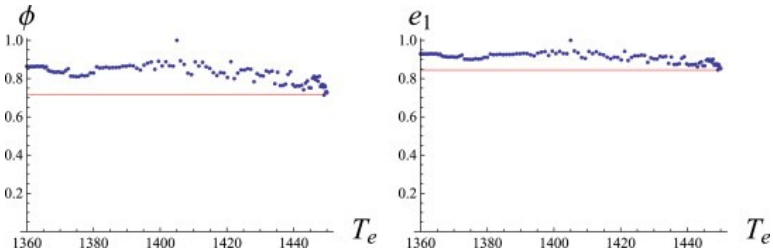

Figure 23 – Fitness variation for the eruption temperature, assuming fixed average values for the water percentage and solidus temperature. The red line marks the lowest value achieved.

The solidus temperature was found to be a significant parameter, producing a worst fit as low as 55%, but the influence of water content is even higher, since in this case the fitness can drop by over

50%; the solidus temperature fitness is also close to being constant for values less than the reference value, while water content has a significant drop on the whole range. The least significant parameter is the eruption temperature, for which the worst case loss is ~30%.

With three independent parameters (H_2O, T_s, T_e) seven Sobol' indices are obtained. The polynomial chaos expansion gives the approximate values shown in Table 5, and the total index for each parameter, as shown in Table 6.

Parameters	Sobol' index (ϕ)	Sobol' index (e_1)
H_2O	0.3834	0.3836
T_s	0.1843	0.1882
T_e	0.1004	0.0916
H_2O, T_s	0.2303	0.2448
H_2O, T_e	0.0698	0.0640
T_s, T_e	0.0281	0.0235
All	0.0038	0.0043

Table 5 – Sobol' indices for all the parameter combinations. Values are shown for both the Φ and e_1 fitness functions.

Parameters	Total index (ϕ)	Total index (e_1)
H_2O	0.6873	0.6967
T_s	0.4465	0.4608
T_e	0.2020	0.1834

Table 6 – Total sensitivity index for each parameter. Values are shown for both the Φ and e_1 fitness functions.

The values confirm the qualitative analysis of the plots, introducing some additional information, in particular with respect to the combined influence of multiple parameters, indicating that the water content also has a significant influence on the sensitivity of solidus and eruption temperatures independently, to the point that the combined influence of water and solidus temperature is higher than the influence of solidus temperature on its own.

The obtained results indicate water content as the most important factor: the model has a strong direct dependency on this parameter, and additionally water content has a significant impact on the dependency of the model on the solidus temperature, which is the other most significant parameter. The strong interaction between water content and solidus temperature can be explained by

considering the physical model underlying the evolution function of the automaton. Indeed, viscosity is known to be a very significant parameter for the morphology of lava flows, and water content in MAGFLOW is the parameter for the viscosity law (Equation 16).

Effusion rate tests

Although the SA was focused on the rheological and physical parameters of the MAGFLOW model, simulations also rely on other input data, among which effusion rates have been indicated as potentially significant by *Miyamoto and Sasaki* [1997]. Indeed, for a given composition, the discharge rate of lava by a vent is an essential parameter in determining the dimensions of the flow.

For MAGFLOW, effusion rates during an eruption are provided as a sampled curve, with given values of the flux at given times. The data is usually obtained by either field observations or, more recently, also from infrared satellite data [*Vicari et al.,* 2009; 2011a, 2001b; *Ganci et al.,* 2012b], and interpolated linearly between the sampled points.

An analysis of the effect of effusion rates on the model should therefore consider at least two separate aspects: as for the other parameters, the potential error in the estimation of the flux rate at a

given time must be considered, but also the overall trend of the flux rate during the eruption. This led to consider two sets of tests.

In the first set, a systematic relative error in the flux rates provided by satellite data is assumed; by altering the sampled values by a given percentage (up to ±50%), new emplacements with fitness are obtained as shown in Figure 24. It is worth noting that water content once again affects the dependency on the input data. The observed drop in fitness is however always of the same order of magnitude as the variation in flux rates, and often lower.
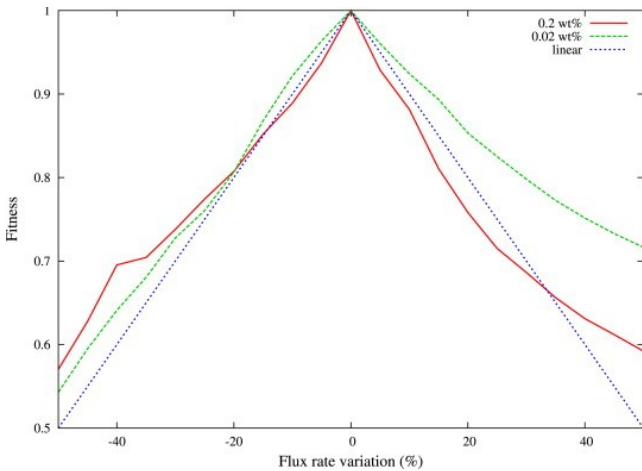

Figure 24 – Variation in fitness (Φ) assuming a systematic relative error in the flux rates estimation, for different values of the water content. An ideal linear decrease in fitness is also shown for comparison.

In the second set of tests, the effect of the effusion rate curve was evaluated by running simulations with three different trends for the effusion rates, all giving the same total amount of emitted lava. The effusion rates provided by satellite data were thus compared with a constant flux rate and a (discretized) Gaussian effusion rate curve (Figure 25).
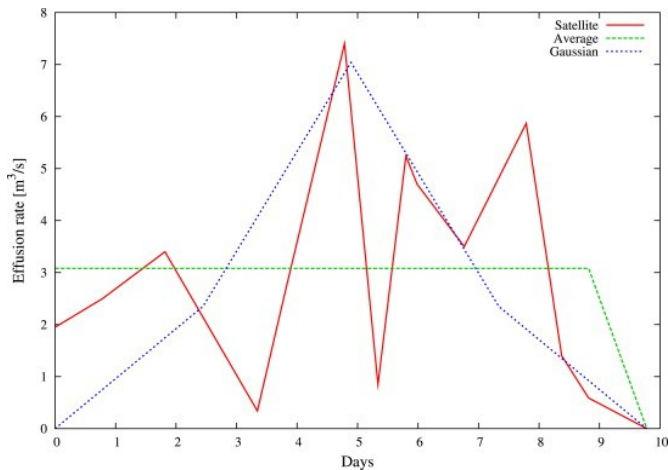

Figure 25 – The different effusion rates with the same total volumes used to test the effect of the effusion rate trend on emplacement.

The results are summarized in Table 7. Since the trend of effusion rates cannot be synthesized as a single quantity, a proper relation

between trend and fitness is difficult to establish. Qualitative considerations highlight however that the trend of the effusion rates can significantly alter the emplacement of the flow, and that once again the effects are more significant with high water contents.

Water content	Flux trend	
	Gaussian	Flat
0.02 wt%	85.56%	64.36%
0.2 wt%	63%	60%

Table 7 – Fitness (Φ) for constant and Gaussian flux for the extremal values of the water content.

By comparing the results of this pair of tests, the most important result that emerges is that the overall trend of the effusion rate can be more important than the individual magnitude of the flux rates: for example, the simple knowledge of the total emitted mass, even if exact, will not provide sufficient information to correctly reproduce a real event, since the lack of knowledge of the flux rates during the eruption can impact the emplacement reducing the fitness by as much as 40%, a drop that would only be matched by errors in the flux rates estimate of 45% or more.

These tests on effusion rate variation confirm the findings of *Miyamoto and Sasaki* [1997] about its relevance for flow emplacement but provide further information, showing that the overall shape of the effusion rate curve can have a much higher impact than the errors in the instantaneous magnitude of the mass flux itself. Combined with the extensive validation done against effusive events [*Vicari et al.,* 2007, 2009, 2011b; *Del Negro et al.,* 2008; *Ganci et al.,* 2012b] on Etna and with the assessed numerical robustness of the implementation, the sensitivity analysis and the effusion rare tests therefore confirm the overall reliability of MAGFLOW for lava flow simulations.

4.3 MAGFLOW input parameters for lava flow simulations

The input parameters required by the MAGFLOW model to simulate the probable lava flow paths are:

- Digital representation of the topography over which the lava is to be emplaced;
- Chemical composition of the lava;
- Estimate of the effusion rate;
- Location of the eruptive vent.

As digital representation of the topography, it was used a DEM of Etna updated to 2005 of 10 m resolution, while for the chemical composition of the lava, the typical material properties of many basaltic rocks available in volcanic regions [*Kilburn and Guest,* 1993, *Harris et al.,* 1997] were chosen (Table 5).

Parameter	Value	Unit of measurement
Density of lava	2600	kg m-3
Specific heat capacity	1150	J kg-1 K-1
Emissivity	0.9	−
Solidification temperature	1173	K
Extrusion temperature	1360	K

Table 8 – Typical parameters for Etna lava flows used as input parameters for the MAGFLOW numerical simulations.

To estimate the effusion rate, i.e. the rate of discharge controlling how a lava body grows, the six eruptive classes extracted from the characterization of the expected eruptions were used. Since the numerical simulation requires hard upper bounds for duration and

lava volume, a short-medium time and a long time were set to 30 and 90 days, respectively, while 30, 100 and 200 × 10^6 m^3 were fixed for the total volume of lava emitted. Crossing these values of duration/volume, six possible curves representing the variation of flux rate in relation to the time of eruption were obtained. As introduced in Paragraph 3.1, the class characterized by a duration of 30 days and a lava volume of 200 × 10^6 m^3 was maintained as a unlikely future extreme event.

The shape of the effusion rate curves has been considered as a kind of bell [*Vicari et al.,* 2007] that starts from a null value of flux rate, reaches the peak after a 1/4 of the entire time of simulation and then gradually decreases until the end of the eruption (Figure 26). In order to avoid an ideal trend for all simulations, a small random perturbation was performed to the effusion rate curves.

Finally, the locations of the eruptive vents are the nodes of the regular grid defined in Figure 5. From these potential vents, six simulations were executed, each one representative of a particular eruptive class and characterized by its own effusion rate.
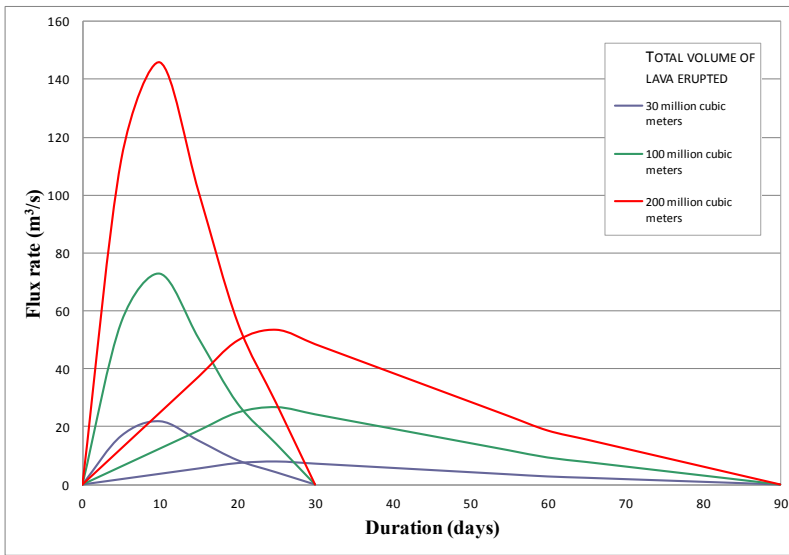
Figure 26 – Curves of flux rate-days for the MAGLFOW numerical simulations associated to the six expected eruptive classes defined in Paragraph 3.2.

Chapter 5

Computation of the hazard map by lava flow invasion

The assessment of the long-term hazard related to lava flow at Mount Etna rests on the integration of all products described in the previous Chapters, including the spatiotemporal probability for the future opening of new eruptive vents, the occurrence probabilities for each class of expected eruptions and the overlapping of MAGFLOW numerical simulations.

The resulting hazard map highlights the probability for each point of the study area of being affected by at least a lava flow during the next fifty years.

5.1 Probabilistic modelling of lava flow hazard

The long-term hazard map related to the lava flow invasion specifies the total accumulation probabilities calculated as the union of individual probabilities of each eruptive event.

Over a certain period of activity, the different eruptive scenarios are independent but not mutually exclusive since they can all occur and have no influence on each other [*Bonadonna,* 2006]. From the probability theory, let A_1, A_2, …, A_n independent events. Then the probability of their union can be calculated as the probability of the intersection of all the complements $A_1{}^C$, $A_2{}^C$,..., $A_n{}^C$. Hence

$$P(A_1 \cup A_2 \cup ... \cup A_n) = P(A_1^C \cap A_2^C \cap ... \cap A_n^C) =$$
$$= 1 - P(A_1^C) * P(A_2^C) * ... * P(A_n^C) =$$
$$= 1 - \prod_{i=1}^{n}(1 - P(A_i)) \tag{19}$$

being $1 - P(A_i)$ the probability that the event i does not occur and $\prod_{i=1}^{n}(1 - P(A_i))$ the probability that none of the n events occur.

In case of lava flow hazard, the total accumulation probability in the considered time interval *Δt for* each point *(x,y)* of the study area can be rewritten as:

$$Haz(x, y, \Delta t) = 1 - \prod_{i=1}^{M}(1 - p_a(v_i, \Delta t) * p_e(v_i)) \qquad (20)$$

where M is the number of simulations of the eruptive class e emitted by vent v_i that invade the point (x,y), $p_a(v_i, \Delta t)$ is the spatiotemporal probability of opening for vent v_i, and $p_e(v_i)$ is the probability of occurrence in v_i for the eruptive class e.

Thus the value *Haz(x, y, Δt)* represents the probability of each point (x,y) to be affected by a lava flow during the next *Δt* years.

5.2 Results

The lava flow hazard map at Mt Etna constructed using the described methodology is reported in Figure 27.

It is based on about 30.000 simulations of lava flow paths starting from 4818 different potential vents. Being a probabilistic long-term hazard assessment, a forecasting period of 50 years was chosen. Hence, the value assigned to each point of the grid represents the probability of being affected by a lava flow emitted by a flank eruptive vent during the next 50 years. Since the summit activity was not investigated, the summit zone is shadowed by a circle area with a radius of 2 km from the central crater.
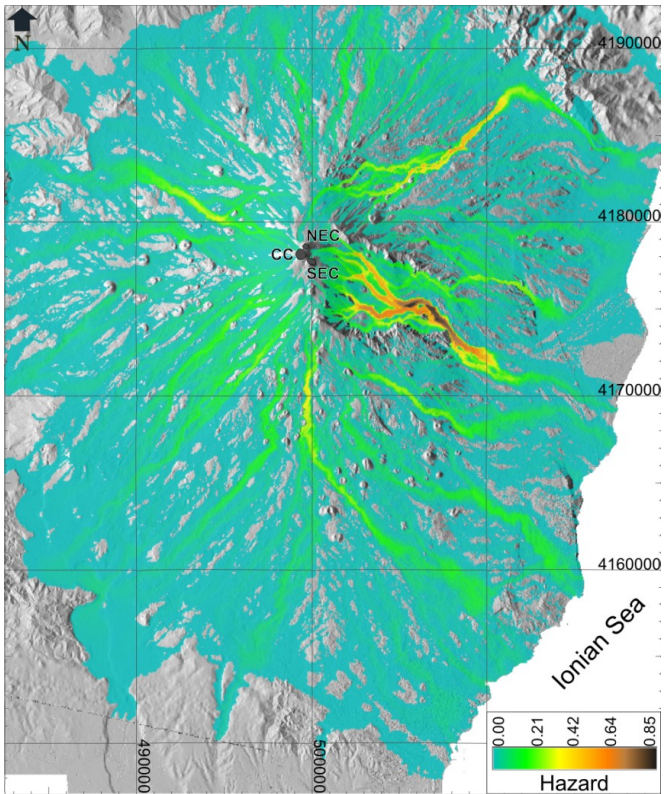
Figure 27 – Hazard map by lava flow invasion at Mt Etna. Summit craters are masked because their activity was separately investigated.

The hazard map in Figure 27 shows a high level of description, ranging continously between zero and the upper extreme (0.85). Notwithstanding, for many practical applications, it is usually more appropriate to consider a lowered number of hazard levels. For this

reason, we also report a discretized representation of the map shown in Figure 27 using a semilogarithmic scale (Figure 29) in order to enable its better readability.
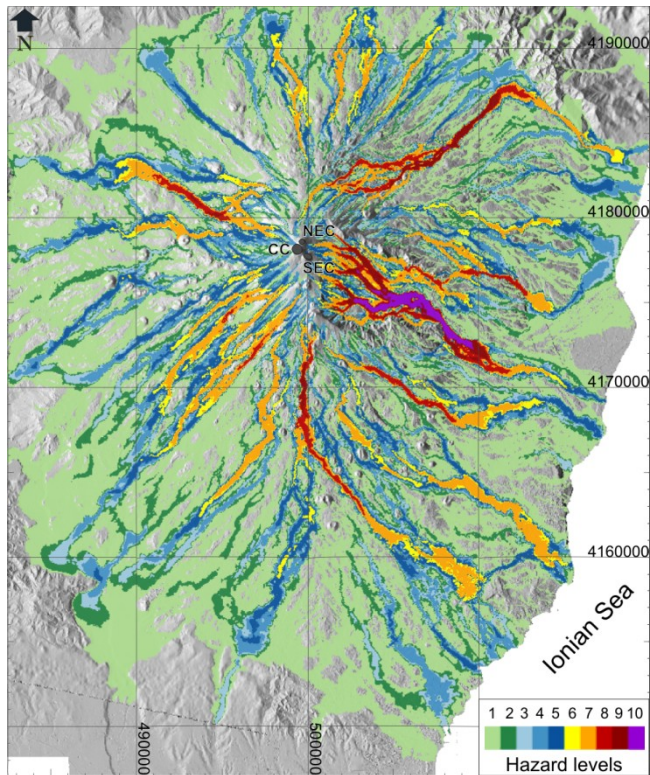

Figure 29 – Discretized lava flow hazard map of Mt Etna. Colors represent different hazard levels indicating for each corresponding area a range of probability to be invaded by a flank eruption in the next 50 years. Summit craters are masked because their activity was separately investigated

Even not included in the study, it is evident from Figure 27 that the touristic facilities located above 1,800 m of altitude (Rifugio Sapienza and Piano Provenzana areas; see Figure 8) are the zones more exposed to lava invasion.

The most densely urbanized sector threatened by lava flow invasion is the southern flank, where major population centres (Nicolosi, Pedara, Trecastagni, and Ragalna) lie distributed between 500 and 1,000 m altitude, at a distance of ~14 km only from the volcano summit (Figure 28).

Figure 28 – Aerial view (from South to North) of the densely urbanized southern flank of Etna. Numerous historical and pre-historical parasitic cones are surrounded by towns and villages

Other towns located in the same South Rift, but at lower elevations, are equally threatened by lava flow invasion, though the hazard progressively diminishes at greater distances from the centre of the volcano.

The towns on the eastern flank are in part "protected" from lava flows by the VdB, a morphological depression (5×7 km wide) able to capture lava flows emitted from the eruptive fissures below the summit craters and along the upper portions of the South and East-North-East Rifts. Only eruptions of exceptionally long duration (months to years) and very high eruption rates (>30 m^3/s) could form lava flows capable of travelling across the entire valley and seriously threaten the population centres of the eastern sector (as Fornazzo in 1979 and Zafferana Etnea in 1992).

The eruptions in the northern sector are generally short but violent, and originate from rather long fractures (>6 km in length). The main population centres exposed to lava invasion are Randazzo and Linguaglossa, downslope of the North-East Rift, and Piedimonte and Sant'Alfio, which lie below the East-North-East Rift. As for the western flank of Etna, the only town lying within the ideal trajectory of lava flows emitted from the West Rift is Bronte, whereas Adrano and Paternò are more remote and thus at considerably lower hazard.

5.3 Retrospective validation of the hazard map

The validation of the lava-flow hazard map is the last crucial step of the whole process, as this provides a quantitative evaluation of its reliability. As the only available knowledge regards the historical information, a retrospective approach is proposed [*Cappello et al., 2011b*] that uses the more recent past eruptions as the potential future events.

The strategy is based on the following concept: if the invasion probabilities reflect the past lava flows, then it is reasonable that they will also predict the areas that will be most likely to be invaded in the future. Hence, the comparison can evaluate the probability distribution of lava-flow hazards at the reference time against the historical lava-flow paths that occurred successively.

As already explained in the back analysis for weights selection (Paragraph 1.2), the available dataset was divided in two parts, learning and testing, using the time barrier 1981 as separator.

The learning dataset was used to calculate the spatiotemporal probability of vent opening $p_a(v_i, \Delta t)$ for a forecasting period Δt of 30 years (Equation 10), and the occurrence probabilities for each eruptive class $p_e(v_i)$ (Equations 11-12).

The resulting lava flow hazard map up to 1981 is thus compiled by taking into account both information on the defined probabilities, p_a

and p_e, and the overlapping of MAGFLOW simulations. Finally a semilogarithm scale was used to discretize the map in ten hazard levels.

The testing dataset consists of the flank eruptions occurred after 1981. To evaluate the overlap with the hazard classes, the actual lava flow fields of these eruptions were superimposed on the map (Figure 30) and two validation scores were defined.

The first index VI_1 represents the percentage of hit the highest hazard classes. Therefore best fit corresponds to 100%. It was defined as:

$$VI_1 = \frac{100}{C*p_{max}}\sum_{i=1}^{N}(C_i * p_i) \qquad (21)$$

where C is the total number of pixels covered by the actual lava flow fields, C_i and p_i are respectively the amount of C and the probability level of the i-th hazard class, p_{max} is the highest hazard value and N is the total number of hazard classes.

The probabilities p_i were established as the upper limits of the intervals on the semilogarithm scale used to discretize the map. Specifically, p_1=0.01, p_2=0.02, p_3=0.03, p_4=0.05, p_5=0.08, p_6=0.1, p_7=0.2, p_8=0.3, p_9=0.5, p_{10}=p_{max}=0.61.
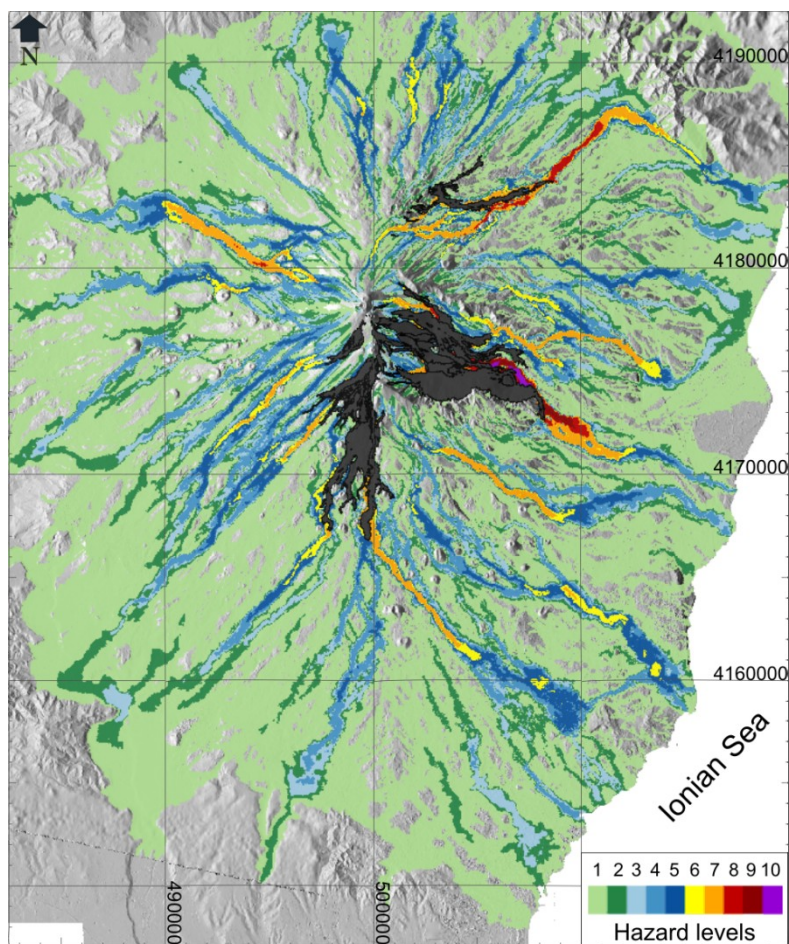
Figure 30 – Lava-flow hazard map built using the learning dataset with superimposed the actual lava-flow paths of eruptions occurred after 1981 (in black). The colors represent different levels of lava-flow invasion hazards.

The value found for VI_1 was 20.2, which is not really significant as it only depends on the extension of the highest hazard class, not on the expected distribution of all the classes.

For this reason, another validation index VI_2 was introduced, representing the mean distance between the observed and expected distributions for each hazard class. VI_2 is 0 if the values provide a perfect fit, while it increases when the discrepancy arises:

$$VI_2 = \frac{1}{N}\sum_{i=1}^{N}\left|\frac{C_i}{C} - \frac{T_i}{T}\right| \tag{23}$$

with C, N, C_i and p_i defined as for VI_1; T_i the number of pixels of the whole map fallen in the i-th hazard class and T the total number of pixels covered by simulations. Thus VI_2 estimates how much the distribution of the most recent lava flow fields is coherent with the distribution of the whole hazard map. The value obtained for VI_2 is 0.09, proving the good reliability of the methodology.

5.4 Discussions

Validation is a decisive step to verify the reliability of a process and to provide a degree of assurance that the results are consistent.

Ideally, the validation should include further independent experiments run forwards in time and involving a significant number of events to make the statistical tests valid. Since further forward studies are unworkable from a scientific point of view, the only chance to validate the final product of a process is to re-use the datasets from which it was derived.

In case of the lava flow hazard assessment, the retrospective validation constitutes a plausible approach looking at what happened in the past for trying to predict what will happen in the future. Nevertheless, applying the retrospective validation to derive the two quantitative indices gives an evaluation not really of the hazard map, but to the methodology developed to elaborate it.

Moreover, the simulations used to generate the lava flow invasion hazard map up to 1981 were performed on DEM updated to 2005. From a statistical point of view, this mismatch should not cause any large variation in the results of the two validation indices. However, for some specific eruptions, the solidified lava could represent a limiting factor, or even a barrier, and therefore changed the time-space evolution of the simulated lava flows.

Chapter 6

Frontiers: the lava flow invasion risk map

A volcanic risk represents any potential loss, damage, or negative impact which can be incurred by people or property as a result of a volcanic hazard.

While a volcanic hazard refers to the probability that a given area will be affected by a potentially destructive volcanic process [*Fournier d'Albe,* 1979], a volcanic risk is the measure of the probability that damage to life, health, property, and/or environment will occur as a result of a given hazard [*Fournier d'Albe,* 1979].

Various volcanic process are potentially dangerous, i.e. volcanic earthquakes, directed blast, tephra, volcanic gases, lava flows, debris

avalanches, landslides, tsunamis, pyroclastic surge, pyroclastic flows, lahars. In the past five centuries, more than 200,000 people have died due to volcanic eruptions [*Tilling,* 1980]. This number is grown especially during the past century (about 845 dead people per year between 1900 and 1986) [*Tilling,* 1991] due not to increased volcanism, but to a rising in the amount of people populating the flanks of active volcanoes and valley areas near those volcanoes [*Tilling,* 1991; *Hall,* 1991].

In Italy, several approaches have been developed for the risk assessment, especially for the Campania region, where three explosive volcanoes, Somma-Vesuvius, Campi Flegrei and Ischia are located in highly populated areas [Lirer and Vitelli, 1998; *Pareschi et al.,* 2000; *Lirer et al.,* 2010].

Unlike these volcanoes, Mount Etna is not particularly dangerous for inhabitants living in tows on its slopes, but its eruptive activity can cause significant economic damage.

A risk map at Etna which links the opening of eruptive vents to the expected damage was built by *Favalli et al.* [2009b]. The methodology quantify the risk which affects exclusively existing buildings on the basis of a database of lava flow simulations starting from more than 70,000 potential vents, a probability distribution of

vent location, an empirical relationship for the maximum length of lava flows, and a database of buildings.

This Chapter presents a feasibility study to investigate a broader approach that combines the hazard map by lava flow invasion [*Cappello et al.,* 2011a, 2011b] with the expected value obtained as the average of three kinds of information: the socio-economic index related to individual municipalities of the Etnean area, the land use index and the anthropogenic factors characterizing the area (buildings, roads and railways). The resulting map allows rapidly visualizing the areas in which there would be the greatest amount of losses in case of an eruptive event occurs. For this reason it could be a useful tool for helping local authorities during ongoing eruptions and for the long-term planning of the territory.

6.1 Methodology for the risk assessment

The volcanic risk can be defined as the product of the probability of occurrence of an eruption for the harm that might follow and can be mathematically translated into the following formula [*Fournier d'Albe,* 1979]:

$$R = V \times E \times H \tag{23}$$

where:

- V (Vulnerability) is the propensity of an element, e.g. people, buildings, infrastructure, economic activities, to suffer damage as a result of stresses caused by an event of a certain intensity;
- E (Exposure or Exposed value) is the number of units, or "value" of each of the elements at risk, as human lives or homes, in a given area;
- H (Hazard) is the probability that a phenomenon of certain intensity occurs in a certain interval of time in a given area.

In general, the vulnerability related to people and buildings is always elevated in relation to volcanic phenomena, so the risk is low when the hazard or the exposed value is minimal. The greater is the probability of eruption, the greater is the risk, and likewise, the higher the goods and the population exposed, the greater the damage that may result and hence the risk. For this reason, the vulnerability V can be considered as a constant, equal to 1, adducting Equation 23 to be rewritten as:

$$R = E \times H \qquad (25)$$

that is, the risk can be evaluated as the product of the exposed value and hazard.

The exposed value

The exposed value or exposure is the value of each of the elements at risk in a given area, like human lives or inhabited areas.

Here it is evaluated as the average of three factors: (i) the socio-economic index, (ii) the anthropogenic index, and (iii) the land use index.

The *socio-economic or ISTAT* (Italian Institute of Statistics) index describes the socio-economic status of each city and takes into account various factors, such as population, buildings, businesses, institutions, local units and employees by municipality. In particular, per each municipality located in the Etnean area, the following data were collected from the website http://www.istat.it: resident population; resident population daily moving; buildings; companies, institutions, local units and employees; enterprises; local units of businesses and institutions; local units by number of employees and by sector of economic activity; local units of public institutions and common institutional form; local units of non-profit institutions.

 All these data were normalized in function of the municipal area and of the maximum value. Each resulting value was then homogeneously assigned within the municipal bounds (Figure 31).

Figure 31 – The socio-economic or ISTAT index describing the socio-economic status of each village. Different factors have been considered as the population, employees, buildings, businesses, institutions and local units.

The *anthropogenic index* indicates the presence of buildings and/or infrastructures such as roads and railways. It takes a value between zero (complete absence of buildings, roads and railways) and one (maximum presence). Data were collected from the Catania province website (http://www.provincia.catania.it) and from the Italian National Cartographic Portal (http://www.pcn.minambiente.it).

As for buildings, the vectorial digital aerophotogrammetry was converted to the raster format shown in Figure 32.

The value represented by each cell indicates how many buildings are at a limiting distance of 50 meters from the center of the cell. The value of each cell was then normalized using the maximum value so that the values vary between 0 (areas where there are no buildings) and 1 (maximum built-up areas).

The same approach was used to obtain the raster maps for roads and highways (Figure 33), and railways (Figure 34).

Finally the distribution of anthropogenic factors on the territory was obtained through a weighted summation where the building raster has a double weight compared with the raster obtained by the sum of the road and railway rasters (Figure 35).
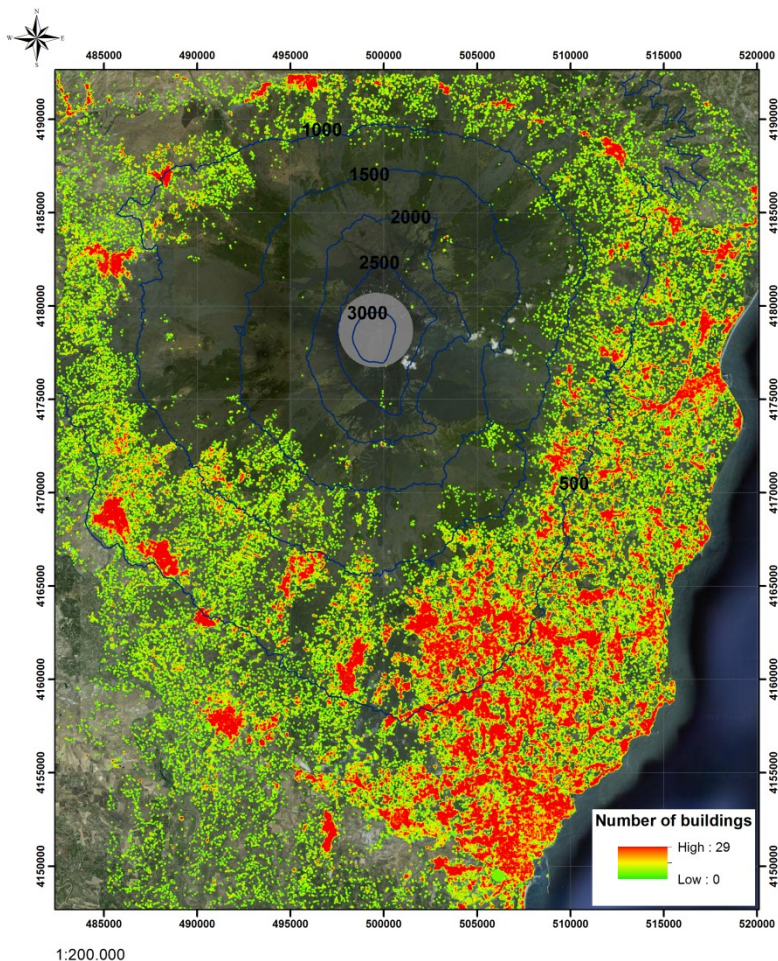
Figure 32 – Raster map obtained converting the vectorial digital aerophotogrammetry of buildings. Summit area is masked because it was not included in the investigation.
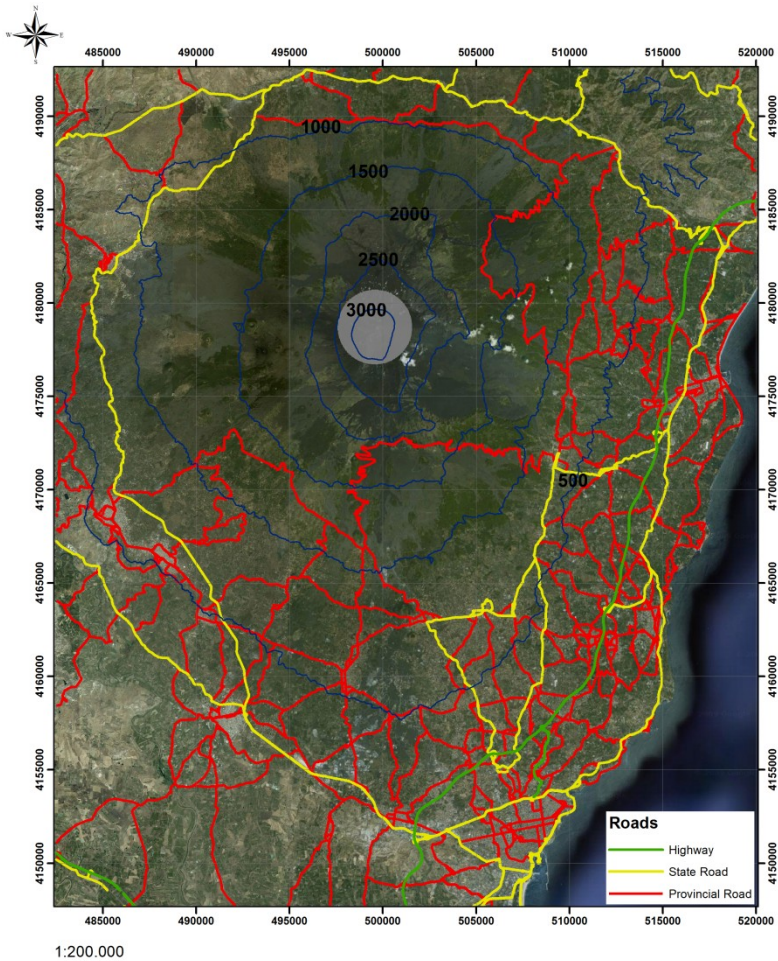
Figure 33 – Raster maps obtained converting the vectorial digital aerophotogrammetry of highways, state roads and provincial roads. Summit area is masked because it was not included in the investigation.
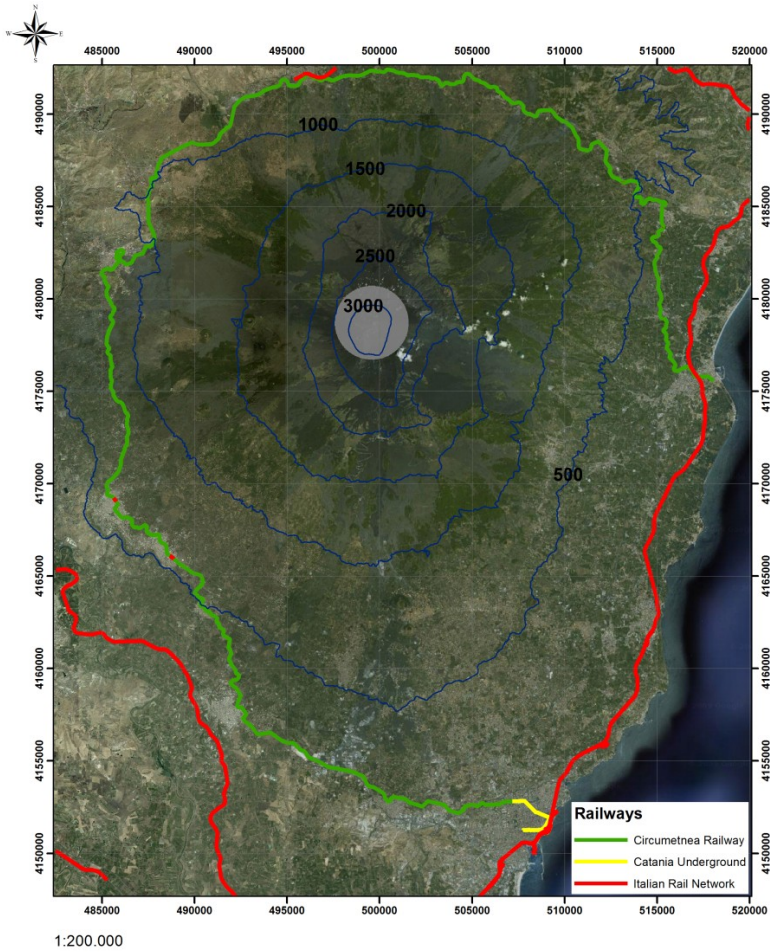
1:200.000

Figure 34 – Raster maps obtained converting the vectorial digital aerophotogrammetry of the Circumetnea railway, Catania underground and the Italian rail network. Summit area is masked because it was not included in the investigation.
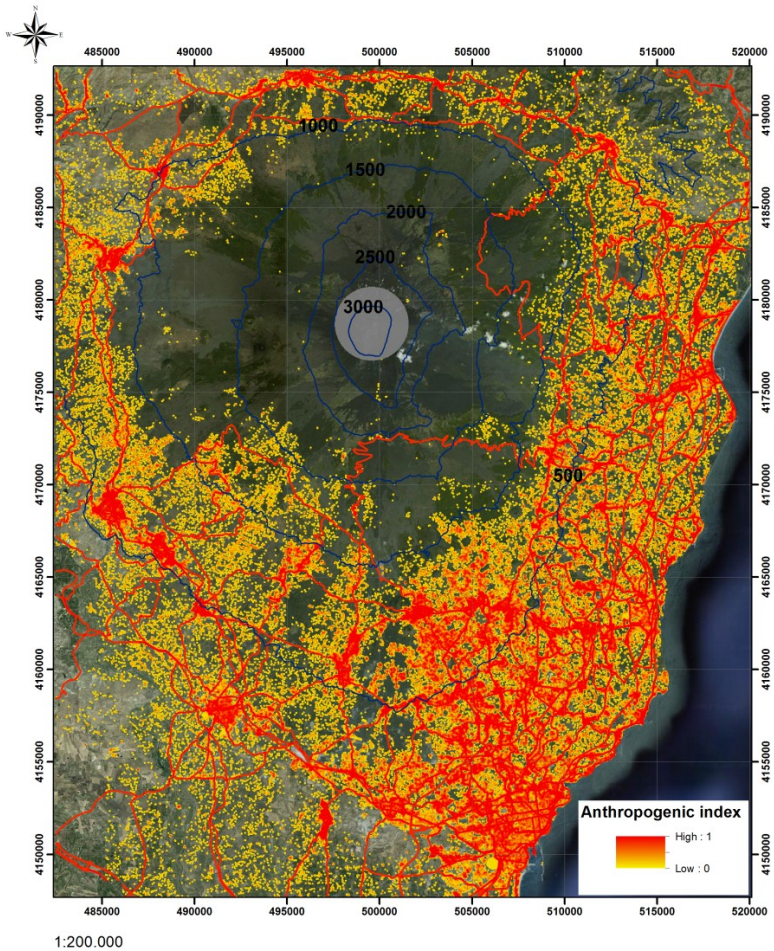
Figure 35 – Raster map showing the distribution of anthropogenic factors obtained by assigning a double weight to the building raster compared with the raster obtained by the sum of the road and railway rasters. Summit area is masked because it was not included in the investigation.

The *land use index* reclassifies the area on the basis of detailed information downloaded from the regional geographic information system of Sicily (http://www.sitr.regione.sicilia.it). Then a weight between 0 and 1 was assigned to the following land use classes:

- fallow, rocky uncultivated, gullies and rocks (0.1 of weight);
- stain and bushy, partially wooded areas or stunted (0.2);
- mixed forest, conifers, broadleaved (0.3);
- simple arable, planted with trees, fodder (0.4);
- pasture, arable land with the presence of vegetables, olives and citrus (0.5);
- woody agricultural enterprises (0.6);
- complex cropping systems, i.e. fruit trees, citrus trees, pistachio trees (0.7);
- industrial areas, general infrastructure (0.8);
- loose urban areas (0.9);
- dense urban areas (1).

The resulting map showing the land classification is reported in Figure 36.

The final exposed value, obtained as the normalized sum of the socio-economic index, the anthropogenic index and the land use index is displayed in Figure 37.
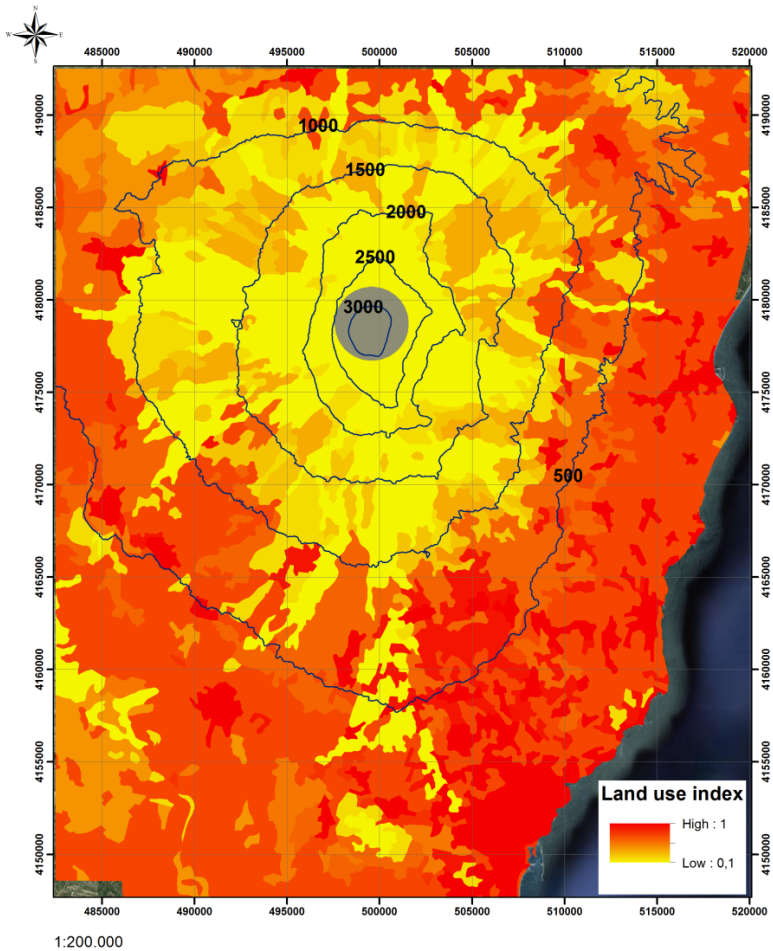
Figure 36 – The land use index obtained by categorizing the territory on the basis of detailed classes, e.g. uncultured, rocks, scrub, woodland, grassland, arable land, cropping systems, industrial areas, urban areas, etc. Summit area is masked because it was not included in the investigation.
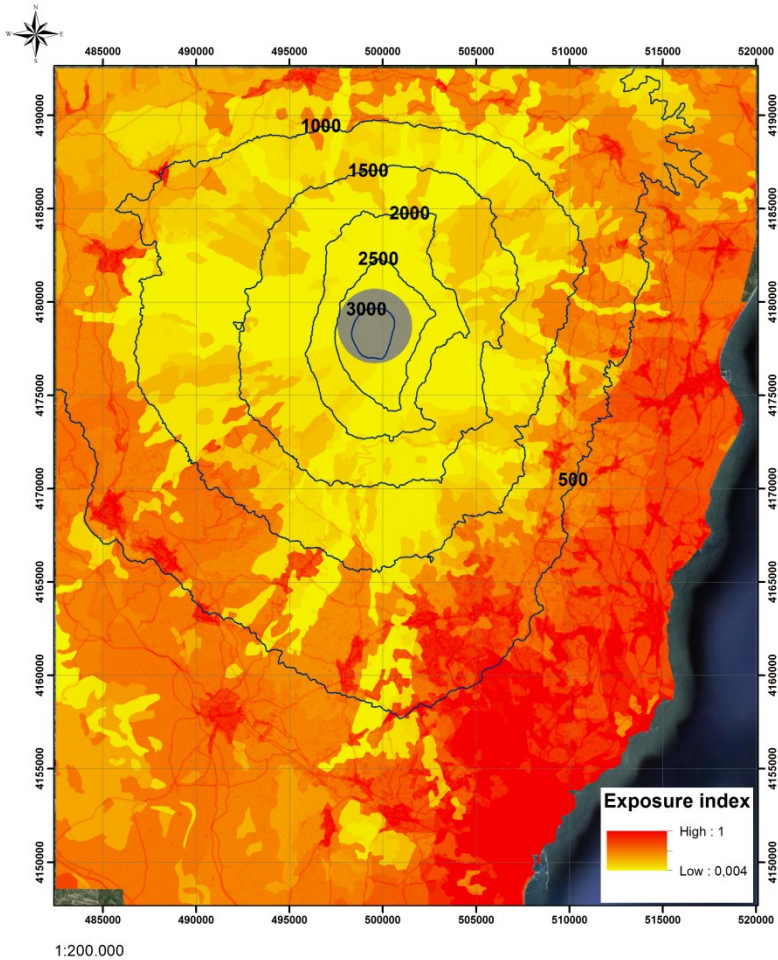
Figure 37 – The exposed value obtained as the normalized sum of the socio-economic index, the anthropogenic index and the land use index. Summit area is masked because it was not included in the investigation.

The hazard map by lava flow

As hazard related to lava flow invasion, the map shown in Figure 27 (obtained combining the spatiotemporal probability map of vent opening; the occurrence probabilities for each eruptive class and the MAGFLOW simulations of lava flow paths) was normalized to obtain an hazard index (Figure 38).
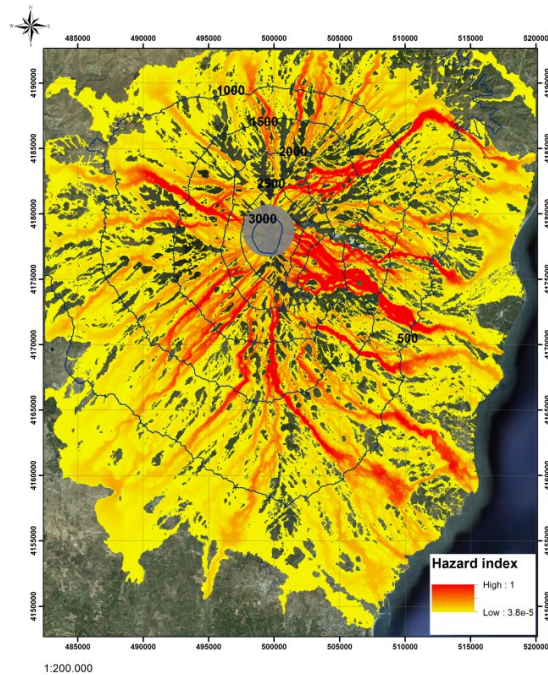

Figure 38 – Hazard map by lava flow invasion normalized between 0 and 1. Summit area is masked because it was not included in the investigation.

6.2 Results

As reported in Equation 25, the risk map by lava flow invasion was obtained multiplying the hazard with the exposed value, calculated as the average of three normalized indices: socio-economic, anthropogenic, and land use.

Figure 39 shows the final map, highlighting the areas worst hit by the lava flows emitted by flank eruptions.

While the highest values of hazard are reached in correspondence of the "Valle del Bove", the highest values of risk regard the inhabited zones. This outcome is influenced by the exposure value present in the calculation of the risk, which considerably smooth the hazard estimates in those areas not urbanized. Especially in "Valle del Bove", which is a rocky and uncultivated depression, the risk of potential loss, damage, or negative impact due to the lava flow invasion becomes almost null.

Comparing the location of the main population centres at Etna with those where the risk is highest, it is evident that the sector most threatened by lava flow invasion is the South-east flank.
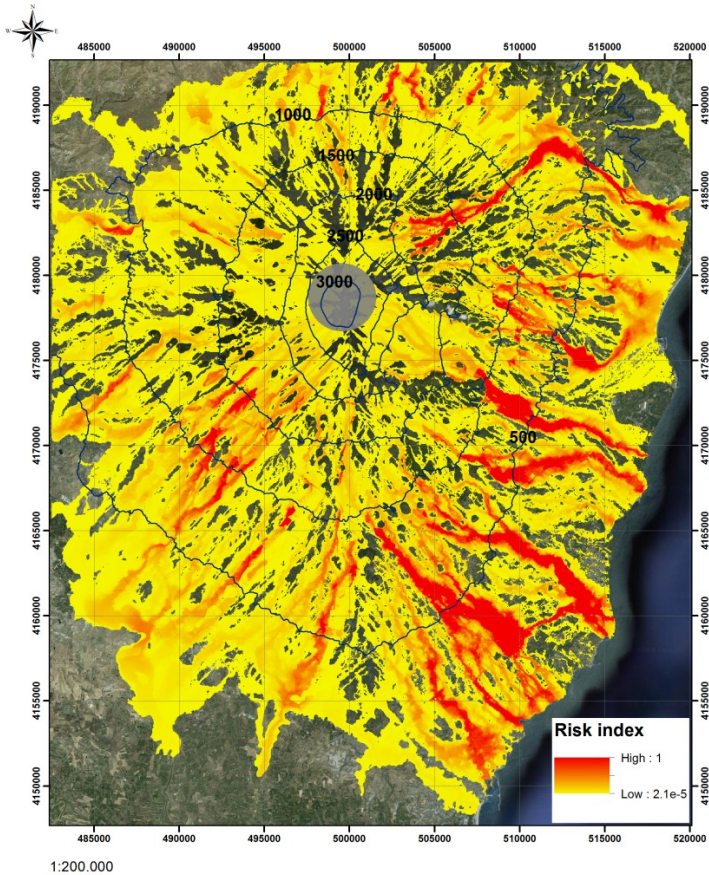
Figure 39 – Risk map obtained by simultaneously considering the characteristics and frequency of eruptive phenomena (through the hazard map) with the social, economic and urban factors (through the exposed value). Summit area (gray area) was excluded from the investigation since summit eruptions do not generally pose risk to towns located on Etna's flanks.

Generally, the South Rift is characterized by eruptions of comparatively long duration (mean duration ~30 days), and greater volumes ($>24\times10^6 m^3$ of lava per eruption), increasing the exposure of urban infrastructures in this sector of Etna to damage. The major population centres at risk by lava flow in the South sector are Nicolosi, Pedara, Trecastagni, and Ragalna, while the risk progressively diminishes in those urban areas at lower elevations of the same sector.

The risk on the eastern flank is partially mitigated by the presence of the VdB, which can capture lava flows formed by eruptive fissures below the summit craters. Only exceptional eruptions in duration or volume could be able to cross the entire VdB and reach the population centres of the eastern sector.

The urban areas on the western and northern sectors can be considered at lower risk. The western flank of Etna is much less urbanized, with only Bronte, Adrano Paternò the only towns potentially at risk. In the northern sector the main population centres exposed to lava invasion are Randazzo, Linguaglossa, Piedimonte and Sant'Alfio.

Conclusions

This thesis provides an original methodology for evaluating the lava flow hazard posed by flank eruptions at Mount Etna yielding significant advances in volcanic hazard assessment procedures. A frontier study has been also proposed with the aim of estimating the risk from lava flow invasion during flank eruptions.

The elevated frequency of the effusive eruptions at Etna prompts the need to analyze in detail the consequences of an eruption and to prepare suitable means to deal with a volcanic emergency. Hazard maps are a powerful instrument to this aim, providing a quantitative evaluation of lava flow hazard in terms of the probability with which a specific area could be potentially reached during a given time window.

Conclusions

The methodology developed for building the hazard map by lava flows is based on a database of MAGFLOW simulations of lava flow paths, constrained by knowledge from former eruptions of Mt Etna. The simulation approach for lava flow hazard assessment provides a more robust and locally accurate analysis than a simple probabilistic approach and accounts for the influence of the actual topography on the path of future lava flows.

The overall reliability of the hazard assessment is strictly influenced by the correctness of the "a priori" assumptions and of the statistical analysis. In particular, the construction of the spatiotemporal probability of vent opening and of the occurrence probability for the eruptive classes constitutes a critical step in the chain of our methodology.

As for the spatiotemporal probability of vent opening, a key point regards the conversion of available datasets into PDFs, since the opening of a new vent can depend on the characteristics of each dataset. Moreover, by assigning an equal probability of occurrence to all performed simulations, a more trivial criterion of hazard mapping is obtained, simply based on the number of simulated events that affect a given zone.

Anyway the flexibility of the developed methodology allows updating the hazard map in a very simple and fast way, as changing

of the input parameters. This means that any uncertainty in assigned probability can be corrected and a new map is obtained simply re-processing the simulations stored in the database.

Knowing the probability of the future course of lava flows is very helpful for the analysis of possible eruptive scenarios and for the development of appropriate measures to minimize the effects of the eruption when the event promises to be very likely. Moreover, knowing the areas that are the most exposed to be invaded by a lava flow is useful for environment preservation and for encouraging better land use planning.

While the hazard map provides the probability that a given area will be affected by a volcanic event, the risk map evaluates the probability that the volcanic event may cause damage to life, health, property and environment in a given area in a certain period of time. Therefore, for a concrete assessment of risk, knowing the hazard is not enough. It is also necessary a careful estimate of the exposed value that is a measure of the seriousness of the effects of a hazardous event in terms of cost.

The risk map presented in this work constitutes the first effort to assess the potential level of risk associated to lava flows by considering both information on historical eruptions and the distribution of goods in the Etnean area. This map may be used as a

guide for managing volcanic emergencies in terms of planning, mitigation of potential effects, relief efforts and to assess the potential loss and replacement costs.

Bibliography

Acocella, V., Neri M. (2003), What makes flank eruptions? The 2001 Etna eruption and its possible triggering mechanisms, Bull. Volcanol., 65, 517-529, doi:10.1007/s00445-003-0280-3.

Acocella, V., Neri, M. (2009). Dike propagation in volcanic edifices: overview and possible developments. Tectonophysics 471:67–77. doi:10.1016/j.tecto.2008.10.002.

Acocella V, Neri M, Scarlato P (2006) Understanding shallow magma emplacement at volcanoes: orthogonal feeder dikes during the 2002–2003 Stromboli (Italy) eruption. Geophys Res Lett 33:L17310. doi: 10.1029/2006GL026862.

Acocella V, Neri M, Sulpizio R (2009) Dike propagation within activecentral volcanic edifices: constraints from Somma-

Vesuvius, Etna and analogue models. Bull Volcanol 71:219–223. doi:10.1007/s00445-008-0258-2.

Allard, P., B. Behncke, S. D'Amico, M. Neri, S. Gambino (2006), Mount Etna 1993–2005: Anatomy of an evolving eruptive cycle, Earth-Science Reviews, 78, 85–114, doi: 10.1016/j.earscirev.2006.04.002.

Alparone, S., B. Behncke, S. Giammanco, M. Neri E. Privitera (2005), Paroxysmal summit activity at Mt. Etna monitored through continuous soil radon measurements. Geophys. Res. Lett., 32, L16307, doi: 10.1029/2005GL023352.

Andronico, D. Lodato, L. (2005). Effusive Activity at Mount Etna Volcano (Italy) during the 20th Century: A Contribution to Volcanic Hazard Assessment, Nat. Hazards, 36, pp. 407–443.

Azzaro R. M. Neri (1992). L' attività eruttiva dell'Etna nel corso del ventennio 1971-1991. Primi passi verso la costituzione di un data-base relazionale, CNR IIV Open File Report, 3, 46 pp.

Baldi, P., E. Bernardo, M. Coltelli, M. Fabris, M. Marsella, C. Proietti A. Sonnessa (2006). La fotogrammetria digitale applicata in aree vulcaniche: l'area sommitale del monte Etna, In: Atti del Convegno ASITA 2006, 10a Conferenza Nazionale delle Associazioni Scientifiche per le Informazioni Territoriali e Ambientali (Bolzano 14-17 novembre 2006), Roma, 149-154.

Bebbington M (2007) Identifying volcanic regimes using Hidden Markov models. Geophys J Int 171:921–942.

Behncke B, Neri M (2003) Cycles and trends in the recent eruptive behaviour of Mount Etna (Italy). Can J Earth Sci 40:1405–1411. doi:10.1139/E03-052.

Behncke, B., M. Neri, R. Carniel, (2003), An exceptional case of lava dome growth spawning pyroclastic avalanches at Mt. Etna (Italy): the 1999 Bocca Nuova eruption. J. Volcanol. Geotherm. Res., 124/1-2 115 – 128, doi:10.1016/S0377-0273(03)00072-6.

Behncke, B., M. Neri, G. Sturiale (2004), Rapid morphological changes at the summit of an active volcano: reappraisal of the poorly documented 1964 eruption of Mount Etna (Italy). Geomorphology, 203-218, doi: 10.1016/j.geomorph.2004.04.004.

Behncke, B., Neri, M., Nagay, A. (2005). Lava flow hazard at Mount Etna (Italy): new data from a GIS-based study. Geological Society of America Special Papers, January 2005, v. 396, 189-208.

Behncke, B., M. Neri, E. Pecora, V. Zanon (2006), The exceptional activity and growth of the Southeast Crater, Mount Etna (Italy), between 1996 and 2001. Bull. Volcanol., 69, 149-173, doi: 10.1007/s00445-006-0061-x.

Bilotta, G., **Cappello, A.,** Hérault, A., Vicari, A., Russo, G., Del Negro, C. (2012). Sensitivity analysis of the MAGFLOW Cellular

Automaton model for lava flow simulation, Environmental Modelling and Software 35, 122-131, doi: 10.1016/j.envsoft.2012.02.015.

Bonaccorso A, Bonforte A, Guglielmino F, Palano M, Puglisi G (2006) Composite ground deformation pattern forerunning the 2004–2005 Mount Etna eruption. J Geophys Res 111:B12207. doi: 10.1029/2005JB004206.

Bonaccorso A, Bonforte A, Calvari S, Del Negro C, Di Grazia G, Ganci G, Neri M, Vicari A, Boschi E (2011) The initial phases of the 2008-2009 Mt. Etna eruption: a multi-disciplinary approach for hazard assessment. J Geophys Res 116:B03203. doi: 10.1029/2010JB007906

Bonadonna C (2006) Probabilistic modelling of tephra dispersal. In: Mader H, Cole S, Connor CB (eds) Statistics in Volcanology. IAVCEI Series Vol. 1, Geological Society of London, 243-259.

Bonforte A, Gambino S, Neri M (2009) Intrusion of eccentric dikes: the case of the 2001 eruption and its role in the dynamics of Mt. Etna volcano. Tectonophysics 471:78–86.

Bonforte A, Guglielmino F, Coltelli M, Ferretti A, Puglisi G (2011). Structural assessment of Mount Etna volcano from Permanent Scatterers analysis. Geochem Geophys Geosyst 12:Q02002. doi: 10.1029/2010GC003213.

Branca S, Coltelli M, Groppelli G (2004) In: Bonaccorso A, Calvari S, Coltelli M, Del Negro C, Falsaperla S (eds) Geological evolution of Etna volcano. Etna Volcano Laboratory, AGU 143,Washington DC, 49–63.

Branca S., Coltelli, M., Groppelli, G., Lentini, F. (2011). Geological map of Etna volcano, 1:50,000 scale, Ital. J. Geosci., 130 (3), 265-291; doi: 10.3301/IJG.2011.15.

Brier, G.W. (1950), Verification of forecasts expressed in terms of probabilities, Mon. Wea. Rev., 78, 1-3, doi: 10.1175/1520-0493(1950)078<0001:VOFEIT>2.0.CO;2.

Burton MR, Neri M, Andronico D, Branca S, Caltabiano T, Calvari S, Corsaro RA, Del Carlo P, Lanzafame G, Lodato L, Miraglia L, Salerno G, Spampinato L (2005) Etna 2004–2005: an archetype for geodynamically-controlled effusive eruptions. Geophys Res Lett 32:L09303, doi: 10.1029/2005GL022527.

Calvari S., M. Neri, H. Pinkerton (2003), Effusion rate estimation during the 1999 summit eruption on Mt. Etna, and growth of two distinct lava flow fields. J. Volcanol. Geotherm. Res., 119/1-4, 107-123, doi: 10.1016/S0377-0273(02)00308-6.

Cappello, A., M. Neri, V. Acocella, G. Gallo, A. Vicari, C. Del Negro (2012), Spatial vent opening probability map of Mt Etna

volcano (Sicily, Italy), Bull. Volcanol., doi:10.1007/s00445-012-0647-4.

Cappello A, Vicari A, Del Negro C (2011a). Assessment and modeling of lava flow hazard on Etna volcano. Boll Geofis Teor Appl 52 (2):299–308.

Cappello A, Vicari A, Del Negro C (2011b) Retrospective validation of a lava flow hazard map for Mount Etna volcano. Ann Geophys 54 (5). doi: 10.4401/ag-5345.

Cardaci C, Coviello M, Lombardo G, Patané G, Scarpa R (1993) Seismic tomography of Etna volcano. J Volcanol Geotherm Res 56:357–368.

Clark J, Evans FC (1954) Distance to nearest neighbour as a measure of spatial relationships in populations. Ecology 35:445–453.

Clocchiatti, R., M. Condomines, N. Guenot, and J. C. Tanguy (2004), Magma changes at Mount Etna: The 2001 and 2002–2003 eruptions, Earth Planet. Sci. Lett., 226, 397–414.

Coltelli, M., C. Proietti, S. Branca, M. Marsella, D. Andronico and L. Lodato (2007). Analysis of the 2001 lava flow eruption of Mt. Etna from 3D mapping, J. Geophys. Res., 112, F02029.

Connor, C.B., and Hill, B.E. (1995). Three nonhomogeneous Poisson models for the probability of basaltic volcanism: Application to

the Yucca Mountain region, Journal of Geophysical Research, 100: 10, 107-10, 125.

Corsaro, R.A., Cristofolini, R., and Patanè, L. (1996). The 1669 eruption at Mount Etna: Chronology, petrology, and geochemistry, with inferences on the magma sources and ascent mechanisms. Bulletin of Volcanology, 58: 348-358, doi: 10.1007/s004450050144.

Crestaux, T., Le Maître, O., Martinez, J.-M. (2009). Polynomial chaos expansion for sensitivity analysis. Reliability Engineering & System Safety 94 (7), 1161-1172.

Crisci, G. M., Avolio, M.V., Behncke, B., D'Ambrosio, D., Di Gregorio, S., Lupiano, V., Neri, M., Rongo, R., Spataro, W. (2010). Predicting the impact of lava flows at Mount Etna, Italy, Journal of Geophysical Research, 115, B04203.

de Figueiredo, L.H., Stolfi, J. (2004). Affine arithmetic: concepts and applications. Numerical Algorithms 36 (1-4), 147-158.

Del Negro, C., Fortuna, L., Herault, A., Vicari, A. (2008). Simulations of the 2004 lava flow at Etna volcano by the magflow cellular automata model, Bulletin of Volcanology, doi: 10.1007/s00445-007-0168-8.

Diggle PJ (1985) A kernel method for smoothing point process data. Applied Statistics. J R Stat Soc Ser C 34:138–147.

Dragoni, M., Bonafede, M., Boschi, E. (1986). Downslope flow models of a Bingham liquid: Implications for lava flows. Journal of Volcanology and Geothermal Research, 30, 305–325.

Falsaperla S, Cara F, Rovelli A, Neri M, Behncke B, Acocella V (2010) Effects of the 1989 fracture system in the dynamics of the upper SE flank of Etna revealed by volcanic tremor data: the missing link? J Geophys Res 115:B11306. doi: 10.1029/2010JB007529.

Favalli, M., Mazzarini, F., Pareschi, M.T., Boschi, E. (2009a). Topographic control on lava flow paths at Mt. Etna (Italy): implications for hazard assessment, J. Geophys. Res., 114, F01019, doi: 10.1029/2007JF000918.

Favalli, M., Tarquini, S., Fornaciai, A., Boschi, E. (2009b) A new approach to risk assessment of lava flow at Mount Etna. Geology, v. 37 no. 12 p. 1111-1114, doi: 10.1130/G30187A.1.

Favalli, M., Tarquini, S., Fornaciai, A. (2011). DOWNFLOW code and LIDAR technology for lava flow analysis and hazard assessment at Mount Etna. Annals of Geophysics, 54(5). doi: 10.4401/ag-5339.

Fournier d'Albe, E.M. (1979). Objectives of Volcanic Monitoring and Prediction. Journ.. Geol. Soc. Lond. 136, 321-326, doi: 10.1144/ gsjgs.136.3.0321.

Ganci G, Harris AJL, Del Negro C, Guehenneux Y, **Cappello A,** Labazuy P, Calvari S, Gouhier M (2012a) A year of lava fountaining at Etna: volumes from SEVIRI. Geophys Res Lett 39:L06305. doi:10.1029/2012GL051026.

Ganci G, Vicari A, **Cappello A,** Del Negro C (2012b) An emergent strategy for volcano hazard assessment: from thermal satellite monitoring to lava flow modeling. Rem Sens Env 119:197–207. doi: 10.1016/j.rse.2011.12.021.

Giammanco, S., K.W.W. Sims, and M. Neri (2007), Measurements of 220Rn and 222Rn and CO^2 emissions in soil and fumarole gases on Mt. Etna volcano (Italy): Implications for gas transport and shallow ground fracture, Geochem. Geophys. Geosyst., 8, Q10001, doi:10.1029/2007GC001644.

Giordano, D., Dingwell, D.B. (2003). Viscosity of hydrous Etna basalt: implications for Plinian-style basaltic eruptions, Bull. Volcanol. 65, 8-14, doi: 10.1007/s00445-002-0233-2.

Guest, J.E. (1973). The summit area of Mount Etna prior to the 1971 eruption. Phil. Trans. Roy. Soc. Lond., A 274, 63-78.

Guest, J.E., and J.B. Murray (1979), An analysis of hazard from Mount Etna volcano, J. Geol. Soc. London, 136, 347–354, doi:10.1144/gsjgs.136.3.0347.

Gwinner, K., M. Coltelli, J. Flohrer, R. Jaumann, K.D. Matz, M. Marsella, T. Roatsch, F. Scholten and F. Trauthan (2006). The HRSC-AX Mt. Etna project: High-resolution orthoimages and 1 m DEM at regional scale, ISPRS Commission I Symposium 36.

Hall, M.L. (1991). Advances (?) in mitigating volcano hazards in Latin America, Earthquakes and Volcanoes, 22 (3), p. 149-150.

Harris, A., Blake, S., Rothery, D., Stevens, N. (1997). A chronology of the 1991–1993 Mount Etna eruption using advanced very high resolution radiometer data: implications for real-time thermal volcano monitoring. J Geophys Res 102, 7985–8003.

Hérault, A., A. Vicari, A. Ciraudo C. Del Negro (2009). Forecasting lava flow hazard during the 2006 Etna eruption: using the MAGFLOW cellular automata model, Computat. Geosci., 35, 1050-1060.

Ho, C-H., Smith, E. I., Feuerbach, D. L., Naumann, T. R. (1991): Eruptive calculation for the Yucca Mountain site, USA: statistical estimation of recurrence rates, Bull. Volcanol., 54, 50-56.

Holcomb, R.T. (1987). Eruptive history and long-term behavior of Kilauea Volcano: in Decker, R.W., Wright, T.L., and Stauffer P. H., (eds.), 1987, Volcanism in Hawaii: U.S. Geological Survey Professional Paper 1350, v. 1, 261-350.

Hughes, J.W., J.E. Guest and A.M. Duncan (1990). Changing styles of effusive eruption on MountEtna since AD 1600, in Magma storage and ascent, edited by M.P. Ryan, 385-406, John Wiley, Chichester.

Imbo, G. (1928), Sistemi eruttivi etnei, Bulletin Volcanologique, Series I, 5: 89–119.

Imbo, G. (1965), Catalog of Active Volcanoes of the World, 28, Italy, IAVCEI, 18: 1-72.

Ishihara, K., Iguchi, M., Kamo, K. (1990). Numerical simulation of lava flows on some volcanoes in Japan. In: Fink, J.H. (Ed.), Lava Flows and Domes: Emplacement Mechanisms and Hazard Implications (IAVCEI Proceedings). Springer-Verlag, 174-207.

Istituto Geografico Militare (1934), Cono Terminale del Monte Etna, Settembre 1932, Anno X. scala 1:5000.

Kilburn, C.R.J., Guest, J.E. (1993). Aa lavas of Mount Etna, Sicily. In: Kilburn, C.R.J., Luongo, G. (Eds.), Active Lavas: Monitoring and Modelling. UCL Press, London, pp. 73–106.

Kiyosugi K, Connor CB, Zhao D, Connor LJ, Tanaka K (2010) Relationships between temporal-spatial distribution of Bull Volcanol (2012) 74:2083–2094 2093 monogenetic volcanoes, crustal structure, and mantle velocity anomalies: an example from

the Abu Monogenetic Volcano Group, Southwest Japan. Bull Volcanol 72:331–340.

Kocabas, V., Dragicevic, S. (2006). Assessing cellular automata model behaviour using a sensitivity analysis approach. Computers, Environment and Urban Systems 30 (6), 921-953.

Lanzafame, G., M. Neri, D. Rust (1996), Active tectonics affecting the eastern flank of Mount Etna: structural interactions at regional and local scale, in Etna: Fifteen years on, edited by P.H. Gravestock and W.J. McGuire, 25-33, Cheltenham and Gloucester College of Higher Education, Centre for Volcanic Research.

Lirer, L., Petrosino, P., Alberico, I. (2010). Hazard and risk assessment in a complex multi-source volcanic area: the example of the Campania region, Italy. Bull Volcanol, 72:411–429, doi: 10.1007/s00445-009-0334-2.

Lutz, T.M., Gutmann, J.T. (1995). An improved method for determining and characterizing alignments of pointlike features and its implications for the Pinacate volcanic field, Sonora, Mexico, Journal of Geophysical Research, 100(B9), 17, pp. 659– 17, 670.

Marti, J., and Felpeto, A. (2010). Methodology for the computation of volcanic susceptibility: an example for mafic and felsic

eruptions on Tenerife (Canary Islands). J Volcanol Geotherm Res 195:69–77.

Martin, A. J., Umeda, K., Connor, C. B., Weller, J. N., Zhao, D., Takahashi, M. (2004). Modeling long-term volcanic hazards through Bayesian inference: an example from the Tohuko arc, Japan. Journal of Geophisical Research, 109(B10208), 1-20.

McGuire, W.J., and A.D. Pullen (1989), Location and orientation of eruptive fissures and feederdykes at Mount Etna; influence of gravitational and regional tectonic stress regimes, J. Volcanol. Geotherm. Res. 38, 325-344, doi:10.1016/0377-0273(89)90046-2.

Miyamoto, H., Sasaki, S. (1997). Role of some parameters on lava flow morphologies. In: Lunar and Planetary Science XXVIII.

Monaco C, De Guidi G, Catalano S, Ferlito C, Tortorici G, Tortorici L (2008) Carta Morfotettonica del Monte Etna. Litografia Artistica Cartografica, Firenze.

Monaco, C., and L. Tortorici (2000), Active faulting in the Calabrian arc and eastern Sicily, J. Geodynamics, 29, 407-424

Moreno, N., Wang, F., Marceau, D. (2008). An object-based land-use cellular automata model to overcome cell size and neighbourhood sensitivity. In: Proceedings of the GEOBIA (Geo-Object Based Image Analysis). University of Calgary.

Mulargia, F., S. Tinti, E. Boschi (1985). A statistical analysis of flank eruptions on Etna Volcano, J. Volcanol. Geotherm. Res., 23, 263–272.

Neri M, and Acocella, V. (2006). The 2004-2005 Etna eruption: implications for flank deformation and structural behaviour of the volcano. J Volcanol Geotherm Res 158:195–206. doi:10.1016/j.jvolgeores.2006.04.022.

Neri M, Guglielmino F, Rust D (2007) Flank instability on Mount Etna: radon, radar interferometry and geodetic data from the southern boundary of the unstable sector. J Geophys Res 112: B04410. doi: 10.1029/2006JB004756.

Neri M, Lanzafame G, Acocella V (2008) Dike emplacement and related hazard in volcanoes with sector collapse: the 2007 Stromboli eruption. J Geol Soc London 165:883–886. doi:10.1144/0016-76492008-002.

Neri M, Casu F, Acocella V, Solaro G, Pepe S, Berardino P, Sansosti E, Caltabiano T, Lundgren P, Lanari R (2009) Deformation and eruptions at Mt. Etna (Italy): a lesson from 15 years of observations. Geophys Res Lett 36:L02309. doi: 10.1029/2008GL036151.

Neri M, Acocella, V., Behncke, B., Giammanco, S., Mazzarini, F., Rust, D. (2011a), Structural analysis of the eruptive fissures at

Mount Etna (Italy). Annals of Geophysics 54(5):464–479. doi: 10.4401/ag-5332.

Neri M, Giammanco S, Ferrera E, Patanè G, Zanon V (2011b) Spatial distribution of soil radon as a tool to recognize active faulting on an active volcano: the example of Mt. Etna (Italy). J Environm Rad 102:863–870. doi:10.1016/j.jenvrad.2011.05.002.

Newhall CG (2000) Volcano warnings, Encyclopedia of volcanoes, edited by H. Sigurdsson, Academic, San Diego, 1185–1197.

Pareschi, M.T., Cavarra, L., Favalli, M., Giannini, F., Meriggi, A. (2000). GIS and volcanic risk management. Nat. Hazards 21 (2 – 3), 361 – 379.

Proietti, C., De Beni, E., Coltelli, M., Branca, S. (2011). The flank eruption history of Etna (1610-2006) as a constraint on lava flow hazard. Annals of Geophysics, 54(5). doi:10.4401/ag-5333.

Romano, R., Sturiale, C., Lentini, F. (1979). Carta geologica del Monte Etna, C.N.R. Italian Geodynamic Project, International Institute of Volcanology, Catania.

Rongo, R., Avolio, M., Behncke, B., D'Ambrosio, D., Di Gregorio, S., Lupiano, V., Neri, M., Spataro, W., Crisci, G. (2011). Defining high-detail hazard maps by a cellular automata approach: application to Mount Etna (Italy). Annals of Geophysics, 54(5). doi: 10.4401/ag-5340.

Rongo, R., Spataro, W., D'Ambrosio, D. (2008). Lava flow hazard evaluation through cellular automata and genetic algorithms: an application to Mt Etna volcano. Fundamenta Informaticae 87 (2), 1-21.

Ruch J., Acocella V., Storti F., Neri M., Pepe S., Solaro G., Sansosti E. (2010). Detachment depth of an unstable volcano revealed by rollover deformation: an integrated approach at Mt. Etna. Geophys Res Lett 37:L16304, doi: 10.1029/2010GL044131.

Salvi F, Scandone R, Palma C (2006) Statistical analysis of the historical activity of Mount Etna, aimed at the evaluation of volcanic hazard. J Volcanol Geotherm Res 154:159–168, doi: 10.1016/j.jvolgeores.2006.01.002.

Sartorius von Waltershausen, W. (1880), Der Aetna, edited by A. von Lasaulx. W. Engelmann, Leipzig, Germany.

Scifoni, S., Coltelli, M., Marsella, M., Proietti, C., Napoleoni, Q., Vicari, A., Del Negro, C.; 2010: Mitigation of lava flow invasion hazard through optimized barrier configuration aided by numerical simulation: The case of the 2001 Etna eruption, Journal of Volcanology and Geothermal Research 192, 16–26.

Siniscalchi A, Tripaldi S, Neri M, Giammanco S, Piscitelli S, Balasco M, Behncke B, Magrì C, Naudet V, Rizzo E (2010) Insights into fluid circulation across the Pernicana Fault (Mt.

Etna, Italy) and implications for flank instability. Journal of Volcanological and Geothermal Research 193:137–142. doi: 10.1016/j.jvolgeores.2010.03.013

Siniscalchi A, Tripaldi S, Neri M, Balasco M, Romano G, Ruch J, Schiavone D (2012) Flank instability structure of Mt Etna inferred by a magnetotelluric survey. J Geophys Res 117:B03216. doi: 10.1029/2011JB008657.

Smethurst, L., M.R. James, H. Pinkerton, J.A. Tawn (2009), A statistical analysis of eruptive activity on Mount Etna, Sicily, Geophys. J. Int., 179, 655–666, doi:10.1111/j.1365-246X.2009.04286.x.

Solaro G, Acocella V, Pepe S, Ruch J, Neri M, Sansosti E (2010) Anatomy of an unstable volcano through InSAR data: multiple processes affecting flank instability at Mt. Etna in 1994-2008. J Geophys Res 115:B10405. doi:10.1029/2009JB000820.

Sparks RSJ (2003) Forecasting volcanic eruptions. Earth Planet Sci Lett 210:1–15. doi:10.1016/S0012-821X(03)00124-9.

Sudret, B. (2008). Global sensitivity analysis using polynomial chaos expansions. Reliability Engineering & System Safety 93 (7), 964-979.

Tanguy, J.C., M. Le Goff, C. Principe, S. Arrighi, V. Chillemi, A. Paiotti, S. La Delfa, G. Patanè (2003), Archeomagnetic dating of

Mediterranean volcanics of the last 2100 years: validity and limits, Earth Planet. Sci. Lett., 211, 111–124.

Tibaldi A, Groppelli G (2002) Volcano-tectonic activity along structures of the unstable NE flank of Mt. Etna (Italy) and their possible origin. J Volcanol Geotherm Res 115:277–302.

Tilling, R.I. (1980). Monitoring active volcanoes, USGS Yearbook, fiscal year 1977, reprint, p. 11.

Tilling, R.I. (1991). Reducing volcanic risk: Are we winning some battles but losing the war?, Earthquakes and Volcanoes, 22 (3), 133-137.

Vicari, A., Ciraudo, A., Del Negro, C., Herault, A., Fortuna, L. (2009). Lava flow simulations using discharge rates from thermal infrared satellite imagery during the 2006 Etna eruption. Natural Hazards, 50, 539–550, doi: 10.1007/s11069-008-9306-7.

Vicari, A., Bilotta, G., Bonfiglio, S., **Cappello, A.,** Ganci, G., Hérault, A., Rustico, E., Gallo, G., Del Negro, C. (2011a). LAV@HAZARD: A web-GIS interface for volcanic hazard assessment. Annals of Geophysics, 54, 5, doi: 10.4401/ag-5347.

Vicari A, Ganci G, Behncke B, **Cappello A,** Neri M, Del Negro C (2011b) Near-real-time forecasting of lava flow hazards during the 12–13 January 2011 Etna eruption. Geophys Res Lett 38:L13317.doi:10.1029/2011GL047545.

Vicari, A., Herault, A., Del Negro, C., Coltelli, M., Marsella, M., Proietti, C. (2007). Modeling of the 2001 lava flow at Etna volcano by a cellular automata approach, Environmental Modelling & Software, 22, 1465-1471.

Wadge, G. (1977). The storage and release of magma on Mount Etna, J. Volcanol. Geotherm. Res., 2, 361-384, doi: 10.1016/0377-0273(77)90021-X.

Wadge, G., Walker G.P.L., and J.E. Guest (1975). The output of the Etna volcano, Nature, 255, 385–387, doi: 10.1038/255385a0.

Wadge G, Young PAV, McKendrick IJ (1994). Mapping lava flow hazards using computer simulation. J Geophys Res 99(B1):489–504.

Waltershausen, W.S. (1845-59). Atlas des Aetna, Berlin, Göttingen, Weimar.

Weller JN, Martin AJ, Connor CB, Connor LJ, Karakhanian A (2006). Modelling the spatial distribution of volcanoes: an example from Armenia. In: Mader HM, Coles SG, Connor CB, Connor LJ (eds) Statistics in volcanology. Spec Pub IAVCEI, Geol Soc London, pp 77–88

Worton BJ (1995) Using Monte Carlo simulation to evaluate kernelbased home range estimators. J Wild Manag 59:794–800.